Article

SOURCE DATA | TRANSPARENT PROCESS | OPEN ACCESS

EMBO reports

T cell-dependent bispecific antibodies alter organ-specific endothelial cell–T cell interaction

Patricia Himmels[1,*], Thi Thu Thao Nguyen[2], Maresa Caunt Mitzner[1,3], Alfonso Arrazate[4], Stacey Yeung[1], Jeremy Burton[1], Robyn Clark[4], Klara Totpal[4], Raj Jesudason[5], Angela Yang[6,7], Margaret Solon[5], Jeffrey Eastham[5], Zora Modrusan[7], Joshua D Webster[5], Amy A Lo[5], Robert Piskol[2] & Weilan Ye[1,**]

Abstract

Preclinical and clinical studies demonstrate that T cell-dependent bispecific antibodies (TDBs) induce systemic changes in addition to tumor killing, leading to adverse events. Here, we report an in-depth characterization of acute responses to TDBs in tumor-bearing mice. Contrary to modest changes in tumors, rapid and substantial lymphocyte accumulation and endothelial cell (EC) activation occur around large blood vessels in normal organs including the liver. We hypothesize that organ-specific ECs may account for the differential responses in normal tissues and tumors, and we identify a list of genes selectively upregulated by TDB in large liver vessels. Using one of the genes as an example, we demonstrate that CD9 facilitates ICAM-1 to support T cell–EC interaction in response to soluble factors released from a TDB-mediated cytotoxic reaction. Our results suggest that multiple factors may cooperatively promote T cell infiltration into normal organs as a secondary response to TDB-mediated tumor killing. These data shed light on how different vascular beds respond to cancer immunotherapy and may help improve their safety and efficacy.

Keywords cancer immunotherapy; cell adhesion molecules; endothelial cell; T cell-dependent bispecific antibody
Subject Categories Cancer; Immunology; Vascular Biology & Angiogenesis
DOI 10.15252/embr.202255532 | Received 2 June 2022 | Revised 8 December 2022 | Accepted 9 December 2022 | Published online 9 January 2023
EMBO Reports (2023) 24: e55532

Introduction

Cancer immunotherapy enhances or restores the capacity of the host immune system to recognize and eradicate cancer (Miller & Sadelain, 2015). Therapeutic advances in cancer immunotherapy have rapidly emerged in the past few years. Among these advances are T cell-retargeting approaches such as chimeric antigen receptor (CAR) T cells and CD3-bispecific antibodies, which have shown promising clinical activity in hematological malignancies (Bargou *et al*, 2008; Kalos *et al*, 2011; Brentjens *et al*, 2013; Maude *et al*, 2014; Turtle *et al*, 2016; Kantarjian *et al*, 2017). CD3-bispecific antibodies bridge T cells to tumor cells by binding the T cell receptor (TCR) CD3 subunit and a surface protein expressed on cancer cells, thereby facilitating T cell-mediated killing of target cells, independent from tumor-antigen specificity of the T cell (Li *et al*, 2017). Yet, despite encouraging preclinical data for CD3-bispecific antibodies targeting solid tumors, evidence for clinical efficacy in solid tumors is still scarce (Yu *et al*, 2017; Dahlen *et al*, 2018; Hosseini *et al*, 2021). In addition, adverse events in T cell-retargeting therapies are often limiting the dose required to eradicate tumors (Trivedi *et al*, 2017). One well-documented acute adverse event for T cell-retargeting therapies is cytokine release syndrome (CRS), which is a whole-body reaction manifested in a myriad of symptoms including fever, chills, tiredness, diarrhea, headache, cough, nausea, and vomiting (Brudno & Kochenderfer, 2016; Gust *et al*, 2017, 2020; Hay *et al*, 2017). Such extensive symptomatic manifestations imply the involvement of multiple organs, among which liver appears to play a significant role. Preclinical studies in mouse tumor models revealed a transient liver toxicity phenotype within 24 h following TDB treatment, which was resolved 4 days later. This phenotype included multiple necro-inflammatory foci, variable perivascular, and periportal chronic inflammatory infiltrate, as well as focal early necrosis of hepatocytes surrounding the central vein, portal tracks, and within lobules (Lo *et al*, 2021). Furthermore, a single-dose safety study in cynomolgus monkeys using TDB treatment revealed acute and transient off-tumor activity, which is consistent with acute hepatocellular toxicity (Staflin *et al*, 2020). As the

1 Department of Molecular Oncology, Genentech, South San Francisco, CA, USA
2 Department of Oncology Bioinformatics, Genentech, South San Francisco, CA, USA
3 Product Development, Genentech, South San Francisco, CA, USA
4 Department of Translational Oncology, Genentech, South San Francisco, CA, USA
5 Department of Research Pathology, Genentech, South San Francisco, CA, USA
6 GSK-Laboratory for Genomic Research, San Francisco, CA, USA
7 Department of Microchemistry, Proteomics and Lipidomics, and Next Generation Sequencing (MPL-NGS), Genentech, South San Francisco, CA, USA
*Corresponding author. Tel: +1 650 225 5680; E-mail: himmels.patricia@gene.com
**Corresponding author. Tel: +1 650 225 4448; E-mail: ye.weilan@gene.com

aforementioned adverse events pose substantial challenges in the management of cancer patients receiving CAR T-cell and T cell-engaging antibodies therapies (Teachey *et al*, 2016), we believe that minimizing the consequences of cytokine release including liver toxicity will result in better patient care. Therefore, it is prudent to thoroughly characterize how tumors and normal tissues respond to T cell-retargeting therapies.

Endothelial cells (ECs) are a heterogenous population at the intra-organ and inter-organ levels (Augustin & Koh, 2017; Potente & Makinen, 2017). EC heterogeneity manifests as differences in cell morphology, function, gene expression, and antigen composition (Aird, 2007a, 2007b; Potente & Makinen, 2017; Kalucka *et al*, 2020a). Heterogeneity is influenced by vessel sizes, flow patterns, and cellular and molecular composition in the tissues where the blood vessels reside (Aird, 2007a), as well as pathological conditions such as tumor growth (Zhao *et al*, 2018, 2020). Single-cell RNA sequencing analysis revealed that the host tissue has a major influence on EC heterogeneity (Kalucka *et al*, 2020a).

The vascular system is essential for the delivery of oxygen and nutrients throughout the body as well as for waste removal. Furthermore, ECs, which line the interior of all blood and lymphatic vessels, control immune cell trafficking by producing chemoattractant and cell adhesion molecules. Cell adhesion molecules (CAMs) are involved in a broad range of normal physiological processes, including cell–cell interactions and cell migration. CAMs also contribute to pathologies such as cancer, inflammation, and autoimmune disease (Okegawa *et al*, 2004). The expression of CAMs and soluble chemotactic factors in ECs facilitate leukocyte extravasation and migration into the organ parenchyma (Carman & Martinelli, 2015). For example, activated endothelium expresses surface adhesion molecules such as intercellular adhesion molecule-1 (ICAM-1) and vascular cell adhesion molecule-1 (VCAM-1) to promote the attachment of peripheral blood leukocytes to the endothelium (Collins, 1993; Fries *et al*, 1993). In order to further facilitate leukocyte binding, previous studies have shown that endothelial tetraspanins associate laterally with ICAM-1 and VCAM-1 to form endothelial adhesive platforms (EAPs). Tetraspanin CD9 is part of the EAPs and has been shown to enhance leukocyte adhesion and trans-endothelial leukocyte migration (Barreiro *et al*, 2005, 2008; Bailey *et al*, 2011; Franz *et al*, 2016; Reyes *et al*, 2018).

In this study, we used an integrated approach involving immunohistochemistry, flow cytometry, and single-cell RNA sequencing to determine how various endothelial cell subsets in the liver and tumor respond to TDB treatment and thus, impact T cell trafficking. We identified a subset of ECs associated with large vessels in the liver that upregulates a list of genes upon TDB treatment. One of these factors is *Cd9*/CD9, which is readily expressed at baseline in the large liver vessels and is further upregulated upon treatment of tumor-bearing mice with TDB. We showed that CD9 facilitates ICAM-1 to support T cell–EC interaction in response to soluble factors released from a TDB-mediated cytotoxic reaction, while CD9 alone plays a modest role in supporting T cell–EC interaction. Our results suggest that multiple factors may act in concert instead of acting alone to promote T cell infiltration into normal organs as a secondary response to TDB-mediated tumor killing. We believe that a systematic *in vivo* evaluation of the candidate factors reported in this study is required to untangle the mechanisms of TDB-induced T cell redistribution. Overall, our data shed light on how different vascular beds respond to cancer immunotherapy and reveal potential new target(s) that could be leveraged to improve the safety and/or efficacy of TDBs.

Results

Anti-HER2/CD3 TDB treatment promotes acute cytokine release and transient margination

Our studies focused on the early responses in tumors versus livers to TDB treatment because of the rationale outlined above. We utilized the MMTV-HER2 Fo5 mammary tumor transplant model (= Founder5 tumor model, Fig 1A), which has been previously described (Lewis Phillips *et al*, 2008). An anti-HER2/CD3 TDB demonstrated robust single-agent antitumor activity in this model (Fig 1B). A rapid increase in serum cytokine levels upon treatment with CAR-T therapies or CD3-bispecific antibodies treatment has been reported in preclinical and clinical settings (Kochenderfer *et al*,

Figure 1. Anti-HER2/CD3 TDB treatment promotes greater degrees of T cell accumulation in the liver than tumor.

A Schematic of experimental setup. After tumor transplantation, mice were divided into two groups with comparable tumor volume distribution within the range of 350–500 mm^3 and treated with either vehicle control (ctrl) or anti-HER2/CD3 TDB via intravenous (i.v.) injections. Blood and tissue samples were analyzed 6 h, 24 h, and 4 days post treatment.

B Founder5 tumor growth kinetics in control-treated (black) and in anti-HER2/CD3 TDB-treated (red) mice ($n = 7$ mice/treatment), shown as mean (left plot) and individual growth kinetics (right plot).

C Serum cytokine levels from control-treated (black) and anti-HER2/CD3 TDB-treated (red) mice, 6 h and 24 h post treatment ($n = 9$ mice/treatment).

D Quantification of $CD4^+$ (top panel) and $CD8^+$ (bottom panel) T cell counts in peripheral blood samples from mice treated with control (black, $n = 10$) or 0.5 mg/kg anti-HER2/CD3 TDB (red, $n = 9$), 24 h post treatment.

E, F Flow cytometry analysis of $CD45^+$ cells and T cells ($CD4^+$ and $CD8^+$) in dissociated tumors normalized to tumor weights (E, $n = 8$ mice/treatment) or dissociated livers normalized to liver weights (F, $n = 9$ mice/treatment), 24 h post treatment.

G, H Representative images of tumor (G) or liver (H) sections from the Founder5 model stained with CD3 (red), Endomucin (white), and DAPI (blue). Right panels: quantification of $CD3^+$ cell counts in Founder5 whole tumor (G) or liver (H) sections normalized to tissue areas. All samples were analyzed 24 h post treatment, $n = 8/9$ mice/treatment. Scale bar = 200 μm.

I, J Tumor (I) or liver (J) tissue cytokine levels normalized to total protein concentration from control-treated (black) and anti-HER2/CD3 TDB-treated (red) mice, 24 h post treatment ($n = 8$ mice/treatment).

Data information: Black = control-treated mice. Red = anti-HER2/CD3 TDB-treated mice. Mann–Whitney test was run to determine *P*-values for experiments with two groups, and Kruskal–Wallis one-way ANOVA was used for multiple groups. Data are shown as means ± SEM (standard error of the mean). ROI, region of interest.
Source data are available online for this figure.

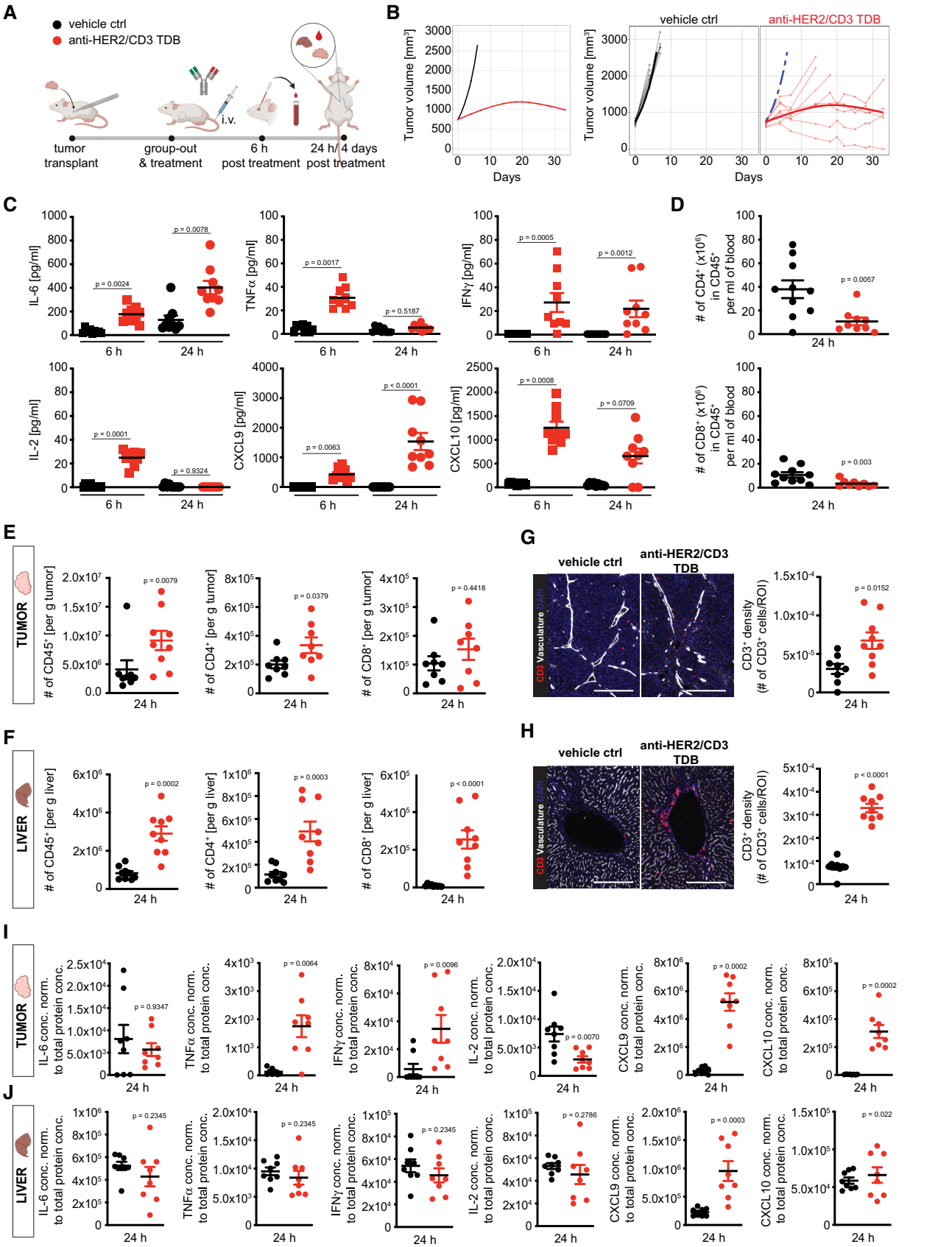

Figure 1.

2012; Teachey *et al*, 2013; Li *et al*, 2018). Consistent with these findings, we observed that anti-HER2/CD3 TDB treatment led to an acute elevation of multiple cytokines and chemokines, including IL-6, TNFα, IFNγ, IL-2, CXCL9, and CXCL10 shortly after TDB administration (Fig 1C), but returned to baseline levels 4 days post treatment with the exception of CXCL9 and CXCL10 (Fig EV1A). These cytokines have been shown to contribute to antitumor efficacy and/or adverse events (Metzemaekers *et al*, 2017; Berraondo *et al*, 2019; Qiu *et al*, 2021). Another phenomenon described in patients and animals upon TDB or CAR-T immunotherapy is the transient loss of circulating lymphocytes, known as margination (Topp *et al*, 2011; Sun *et al*, 2015; Li *et al*, 2017). The mechanism of margination is at present not well understood, but is likely related to systemic changes in cytokines and chemokines. We performed flow cytometric analysis of circulating immune cells in blood samples and consistently observed a transient decrease of T cells to varying degrees within 24 h upon TDB treatment (Fig 1D), likely reflecting a margination response, which is resolved 4 days after TDB treatment (Fig EV1B and C). Collectively, these data confirmed that our model recapitulates similar responses to TDB treatment observed in cancer patients.

Anti-HER2/CD3 TDB treatment promotes greater degrees of acute T cell accumulation in the liver than tumor

T cell accumulation in solid tumors is an important requirement for antitumor activity of T cells and has been shown to correlate with responses to cancer immunotherapies (Pockaj *et al*, 1994; Ji *et al*, 2012; Peng *et al*, 2015; Spranger *et al*, 2015; Chen *et al*, 2016; Wang *et al*, 2016; Li *et al*, 2019). Therefore, we analyzed the effect of TDB treatment on intra-tumoral T cells in dissociated Founder5 tumors by flow cytometry. On average, we observed a 1.5- to 2-fold increase of $CD4^+$ T cells, $CD8^+$ T cells, or $CD45^+$ cells 24 h after TDB treatment in the tumor (Figs 1E and EV1D). It is speculated that temporary lymphocyte margination may be followed by lymphocyte extravasation not only into tumors but also into normal tissues, which is undesirable as it reduces the pool of circulating T cells available for recruitment to the tumor as well as potentially resulting in negative adverse events. We set out to analyze lymphocyte distribution in normal tissues and focused on the liver because of the acute hepatotoxicity observed in preclinical models (Staflin *et al*, 2020). To our surprise, despite the absence of HER2 expression in the liver (Park *et al*, 2017), the magnitude of $CD45^+$ cell and $CD4^+$ T cell accumulation was higher in the liver than the tumor (4.5-fold and 3-fold, respectively). Even more profound was the elevation of liver $CD8^+$ T cells upon TDB treatment (~25-fold increase) (Fig 1F).

We corroborated our flow cytometric results with immunohistochemistry (IHC) analysis. TDB treatment in the Founder5 tumor model led to a modest increase of $CD3^+$ T cells in the tumors within 24 h (Fig 1G). Consistent with the flow cytometric analysis, we found that the acute increase of T cells is more profound in the livers compared to tumors (Fig 1H). Using a dual chromogenic IHC for CD8a and pan-cytokeratin (AE1/AE3) to label tumor cells, we found that the majority of the infiltrating T cells in the tumor and liver were indeed cytotoxic $CD8^+$ T cells (Fig EV1E and F, respectively). When comparing $CD8^+$ T cell infiltration 4 days after TDB treatment, we found an increased number of T cells in the tumor (Fig EV1E), in line with our observation that TDB treatment showed robust antitumor efficacy after several days (Fig 1B). In this model, the number of T cells in the liver returned to the control levels 4 days after TDB treatment (Fig EV1F).

Consistent with the pathology seen in cynomolgus monkeys (Staflin *et al*, 2020), we observed a modest and transient elevation in liver enzyme levels, such as alanine transaminase (ALT) and aspartate aminotransferase (AST) 6 h and 24 h post treatment, which is resolved after 4 days (Fig EV1G). When we compared cytokine and chemokine levels within the tumors and livers, we found that many were acutely increased in the tumor upon TDB treatment, but were mostly unchanged in the liver (Figs 1I and J, and EV1H and I). This finding indicates that the primary response occurred within the tumor, and the liver changes reflect a secondary response to cytokines and chemokines released into circulation.

We confirmed that the effects observed were dependent on the engagement of TDB with T cells and tumor cells, as non-tumor-bearing mice did not show any of these effects with regard to circulating cytokine/chemokines, lymphocyte counts in the liver, or liver enzymes (Fig EV2A–C, respectively). These data also suggest that the acute hepatotoxicity observed in preclinical models is most likely not due to drug-induced hepatotoxicity or drug-induced liver injury (DILI). To determine if the increased T cell infiltration into livers is due to vascular activation triggered by intravenous (i.v.) injection, we compared i.v. versus intraperitoneal (i.p.) TDB administration and found no significant difference with regard to the changes in ALT/AST levels, cytokine/chemokine levels, and lymphocytes counts (Fig EV2C–E, respectively).

Interestingly, when we further analyzed the T cell phenotype in the liver versus tumor tissues (Fig 2A), we observed that T cells ($CD8^+$ and $CD4^+$ T cells) in the tumor showed an activation pattern (upregulation of $CD69^+$ and $GZMB^+$ in T cells; Fig 2B and C upper panels) consistent with T cell-receptor (TCR) engagement. However, T cells in the liver did not show this type of activation (Fig 2B and C lower panels). In line with this finding, T cells in the tumor showed

Figure 2. T cell phenotypes differ in tumor and liver upon TDB treatment.

A Gating strategy for flow cytometry analysis of T cells. Singlets are gated based on forward scatter area (FSC-A) versus forward scatter height (FSC-H). $CD45^+$ cells are gated from viable cells, and T cells are sub-divided as $CD8^+$ versus $CD4^+$ T cells from viable cells and $CD45^+$ cells. T cells are further gated for proliferation status ($Ki67^+$), activation status ($CD69^+$ or $GZMB^+$), or T cell subtypes ($T_{eff/em}$: $CD44^{hi}$ $CD62L^{low}$; T_{cmem}: $CD44^{hi}$ $CD62L^{high}$; $T_{naïve}$: $CD44^{low}$ $CD62L^{high}$). Eff/em, effector/effector memory; cmem, central memory.

B, C Flow cytometry analysis of T cell phenotype and T cell subsets for $CD8^+$ T cells (B) and $CD4^+$ T cells (C) in dissociated tumors normalized to tumor weights (upper panels) or dissociated livers normalized to liver weights (lower panels), 24 h post treatment ($n = 8$ mice/treatment).

Data information: Black = control-treated mice. Red = anti-HER2/CD3 TDB-treated mice. Mann–Whitney test was run to determine *P*-values for experiments with two groups; Kruskal–Wallis one-way ANOVA was used for multiple groups. Data are shown as means ± SEM.
Source data are available online for this figure.

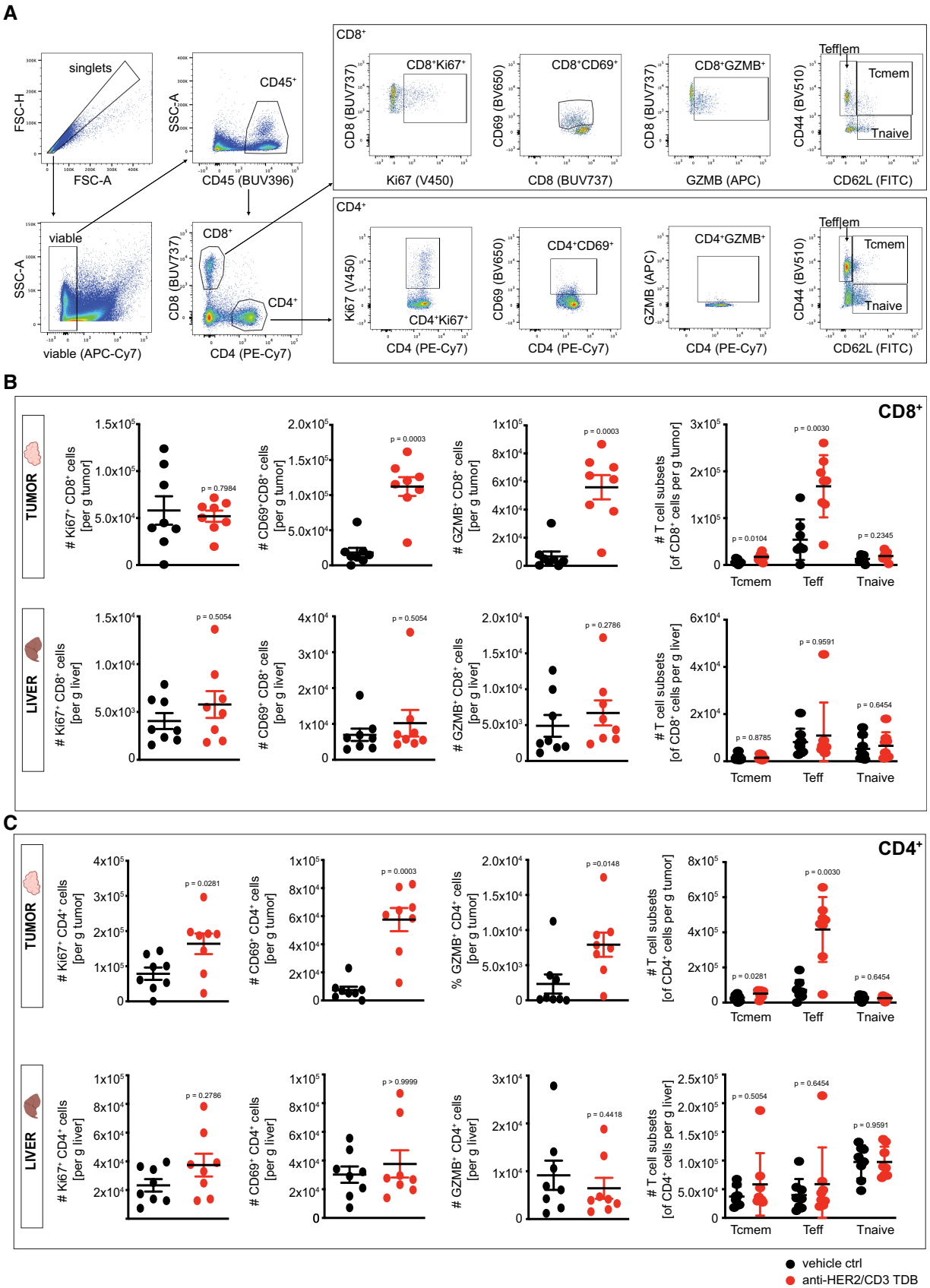

Figure 2.

a shift towards effector T cells, whereas no shift in T cell subpopulations was observed in the liver. Proliferation was only observed in the $CD4^+$ T cells in the tumor (Fig 2B and C). Taken together, our results strongly argue that T cell accumulation in the liver is a secondary response to TDB-mediated T cell activation in the tumor and the subsequent release of cytokines and chemokines into circulation.

The finding that TDB-induced T cell accumulation in the liver was greater than in the tumor was confirmed in another tumor model: mice harboring ID8 ovarian cancer overexpressing a surface molecule LYPD1 and treated with an anti-LYPD1/CD3 TDB (Lo *et al*, 2021). In this model, we also observed an acute response as circulating cytokines and chemokines were elevated shortly after TDB treatment but resolved 4 days after TDB treatment (Fig EV3A). In addition, T cell margination was observed 24 h after treatment (Fig EV3B). Similar to the Fo5 tumor model, we observed T cell accumulation around large vessels in the livers but not in the tumors (Fig EV3C and D). Liver enzyme levels were also acutely increased (Fig EV3E), similar to what we observed in the Fo5 tumor model. In this model, however, we did not observe an increase in tumor-infiltrating T cells, even 4 days after treatment. In summary, our analysis revealed that TDB treatment induces a greater extent of acute T cell accumulation in the liver than in the tumor, which is dependent on the presence of tumors.

TDB treatment leads to EC activation and upregulation of adhesion molecules

We noticed T cell accumulation around large vessel walls in the liver (Fig 1H), indicating potential trafficking across the vascular endothelium. In order to evaluate if TDB-induced circulating molecules promoted T cell–EC adhesion, we set up an *in vitro* assay. This allowed us to mimic to a certain degree our *in vivo* observations but in a more accessible and controlled environment. For this, an anti-CD20/CD3 TDB was added to peripheral blood mononuclear cells (PBMCs) isolated from healthy human blood samples (Fig 3A), leading to B cell killing (CD20-positive) by T cells and the release of various signaling molecules into the culture media, which are similar to the cytokine/chemokines found *in vivo* (Fig 3B). We used this TDB-conditioned PBMC supernatant to stimulate confluent primary ECs, and we observed elevation of adhesion molecules ICAM-1 and VCAM-1 (Fig 3C and D) to a similar extent as treatment with tumor necrosis factor α (TNFα) (Fig 3D), which is known to be a potent stimulant of endothelial cell activation (Liao, 2013). Furthermore, pretreatment of ECs with TDB-conditioned PBMC supernatant led to increased T cell adhesion compared to ECs pre-treated with control PBMC supernatant (Fig 3E and F).

Since TDB-conditioned PBMC supernatant is capable of activating ECs *in vitro* and factors in the supernatant are similar to circulating factors in HER2/CD3 TDB-treated mice, we went on to examine EC activation *in vivo*. TDB treatment significantly upregulated the adhesion molecules ICAM-1 and VCAM-1 in the liver to a greater extent compared to tumor tissues (Fig 4A and B, respectively). Similarly, we observed a greater degree of endothelial activation in the liver than in the tumor in the ID8/LYPD1X4 ovarian cancer model (Fig EV3F and G). Bulk RNA sequencing of matching liver and tumor samples 24 h after treatment also revealed known endothelial transcripts, including adhesion markers (*Icam1*, *Icam2*, *Vcam1*, *Sele*, *Selp*, *Podxl*, *Pdpn*, *Cdh5*, *Mcam*), being upregulated in TDB-treated liver and tumor samples (Fig 4C and D, respectively). Coinciding with the greater degree of T cell accumulation in the liver than in the tumor, the degree of ICAM-1 and VCAM-1 upregulation in the liver was greater compared to the tumor. We then carried out additional analysis of the vasculature in the liver and tumor and found that vessel density was not changed by TDB treatment in either tissue (Fig 4E and F, left panels). We also did not observe a significant change upon TDB treatment when examining pericyte coverage of vessels ($NG2^+$, $Desmin^+$, αSMA^+, $Endomucin^+$) as a readout for vascular stability and maturity (Fig 4E and F, right panels). Interestingly, when correlating pericyte coverage with expression of adhesion molecules, we found that vascular ICAM-1, but not VCAM-1, correlated with mature vessels in the liver (Fig 4G), whereas only vascular VCAM-1 but not ICAM-1 expression on vessels correlated with pericyte coverage in the tumor (Fig 4H). This implies that the composition of vascular subtypes differs between the liver and tumor, and therefore, they responded differently to the TDB-induced systemic factors. In addition, we also measured circulating angiopoietin-2 (ANG2) levels as a surrogate of endothelial cell activation *in vivo* (Fiedler & Augustin, 2006; Scholz *et al*, 2015), and we found that TDB treatment increased the levels of circulating ANG2 (Fig 4I). However, tissue levels of ANG2 were not significantly changed in the liver and tumor (Fig 4J and K, respectively), suggesting that ANG2 release instead of synthesis was changed in response to TDB treatment. These findings implied that the liver vasculature more readily responded to TDB-induced circulating factors and was, therefore, more capable of supporting T cell infiltration than the tumor vasculature.

Anti-HER2/CD3 TDB treatment induces dramatic transcriptional differences in the liver but does not change EC subpopulation identities

We hypothesized that organ-specific EC subtypes may account for the differential T cell accumulation in normal tissues versus tumors in response to TDB. Thus, we set out to identify the molecular response of liver ECs to TDB treatment using single-cell analyses.

Single cells isolated from the liver were processed for single-cell RNA sequencing (scRNAseq) and analyzed. Read alignment, unique molecular identifier (UMI) counting, and low RNA-content cell-filtering were done using the Cell Ranger pipeline (Zheng *et al*, 2017). Cells with high mitochondrial gene counts (> 25%) were removed as lysing/apoptotic cells. Liver tissue samples were analyzed in biological triplicates and were found to equally contribute to each of the clusters, ruling out potential batch effects (Fig EV4A). After performing these quality control (QC) steps, 12,170 liver cells from three control-treated mice and 11,566 liver cells from three TDB-treated mice were analyzed jointly. Through unsupervised clustering, 25 clusters in liver tissue samples were distinguished and visualized using t-distributed Stochastic Neighbor Embedding (tSNE) (Figs 5A and EV4B). Based on the expression of a panel of known markers and cell types from the mouse cell atlas (Han *et al*, 2018), we identified four T cell clusters, one B cell cluster, eight myeloid clusters, and six distinct EC clusters, as well as organ-specific cell types (Kupffer cells 1–5 and hepatocyte) as expected. In addition, we identified one cluster that appeared to be a mixture of ECs and T cells (EC/T cluster), as markers of both cell types were

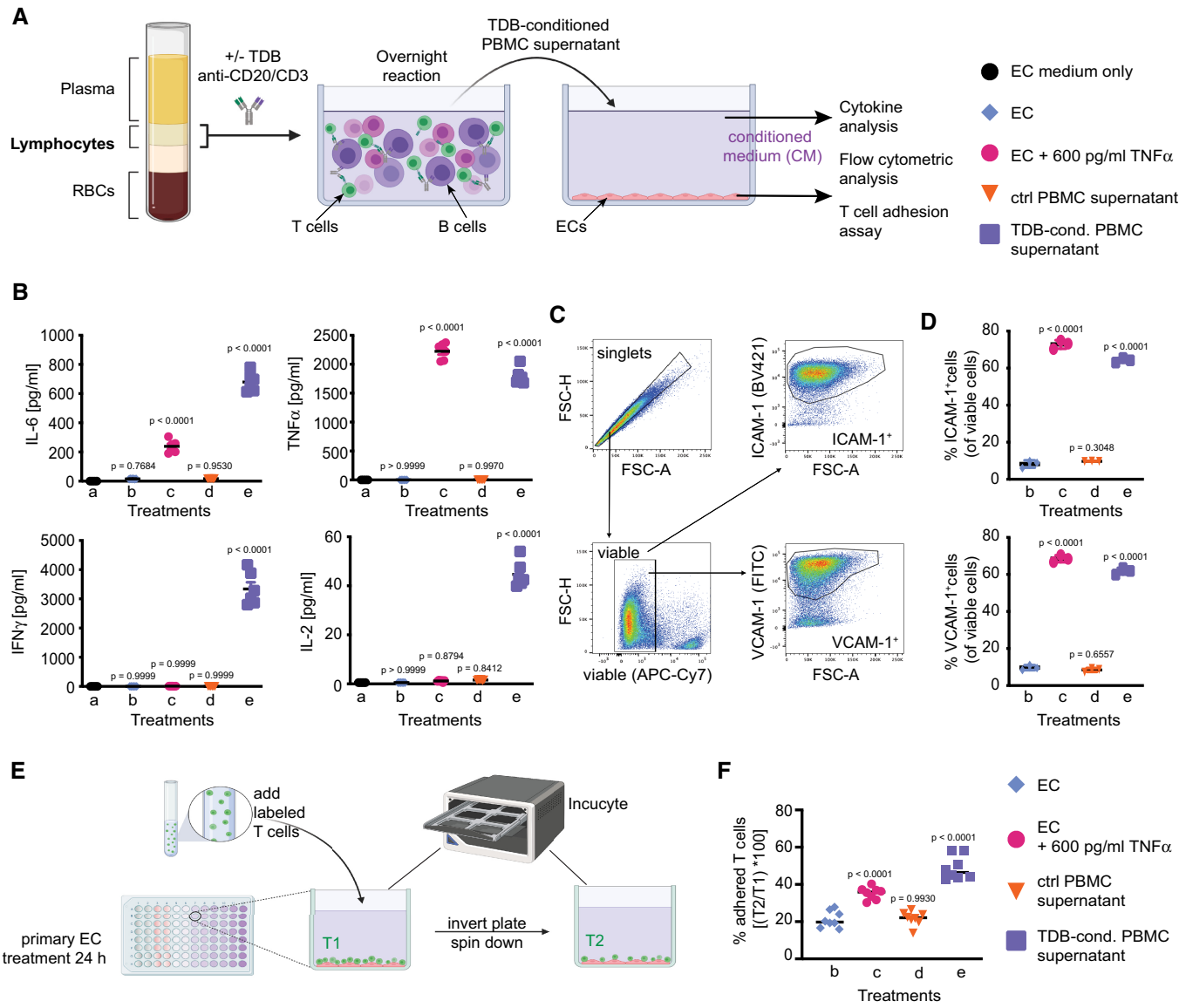

Figure 3. TDB-conditioned PBMC supernatant upregulates adhesion molecules on primary human endothelial cells *in vitro*.

A Schematic of experimental setup for obtaining and using TDB-conditioned peripheral blood mononuclear cell (PBMC) supernatant. Briefly, PBMCs isolated from healthy human blood samples were incubated with or without an anti-CD20/CD3 TDB, and the supernatants were harvested 18 h post treatment. PBMC supernatants were then used to treat primary human umbilical vein endothelial cells (HUVECs).

B Cytokine concentrations in conditioned medium of HUVECs cultured without treatment (blue diamond, treatment b), or with 600 pg/ml TNFα (pink circle, treatment c), or with control PBMC supernatant (orange triangle, treatment d), or with TDB-conditioned PBMC supernatant (purple square, treatment e). All done in $n = 6$ replicates with 6 h incubation. Endothelial cell culture medium alone (black circle, treatment a, $n = 4$) was plotted as reference.

C Gating strategy for flow cytometry analysis of surface expression of ICAM-1 and VCAM-1 on HUVECs. Singlets were gated based on forward scatter area (FSC-A) versus forward scatter height (FSC-H). Activated endothelial cells were gated as ICAM-1$^+$ or VCAM-1$^+$ endothelial cells from viable cells.

D Quantification of percentage of ICAM-1$^+$ (top panel) and VCAM-1$^+$ (bottom panel) endothelial cells with the same treatments as defined in panel (B). All done in triplicates.

E Schematic of experimental setup for T cell–EC adhesion assay. Briefly, confluent HUVECs were treated for 24 h as described in panel (B). T cells were added and allowed to adhere for 3 min, and the unadhered T cells were removed by inverted spin. The percentage of adhered T cells was calculated as: [remaining T cells after inverted spin (T2)/total input T cells (T1)] × 100.

F Quantification of T cell adhesion to a monolayer of HUVECs treated with the same treatments as defined in panel (B). All done in biological triplicates with eight technical replicates per biological replicate.

Data information: HUVECs cultured without treatment (blue diamond, treatment b), or with 600 pg/ml TNFα (pink circle, treatment c), or with control PBMC supernatant (orange triangle, treatment d), or with TDB-conditioned PBMC supernatant (purple square, treatment e). Endothelial cell culture medium alone (black circle, treatment a). Ordinary one-way ANOVA was applied. Data are shown as means ± SEM. EC, endothelial cell; RBCs, red blood cells.
Source data are available online for this figure.

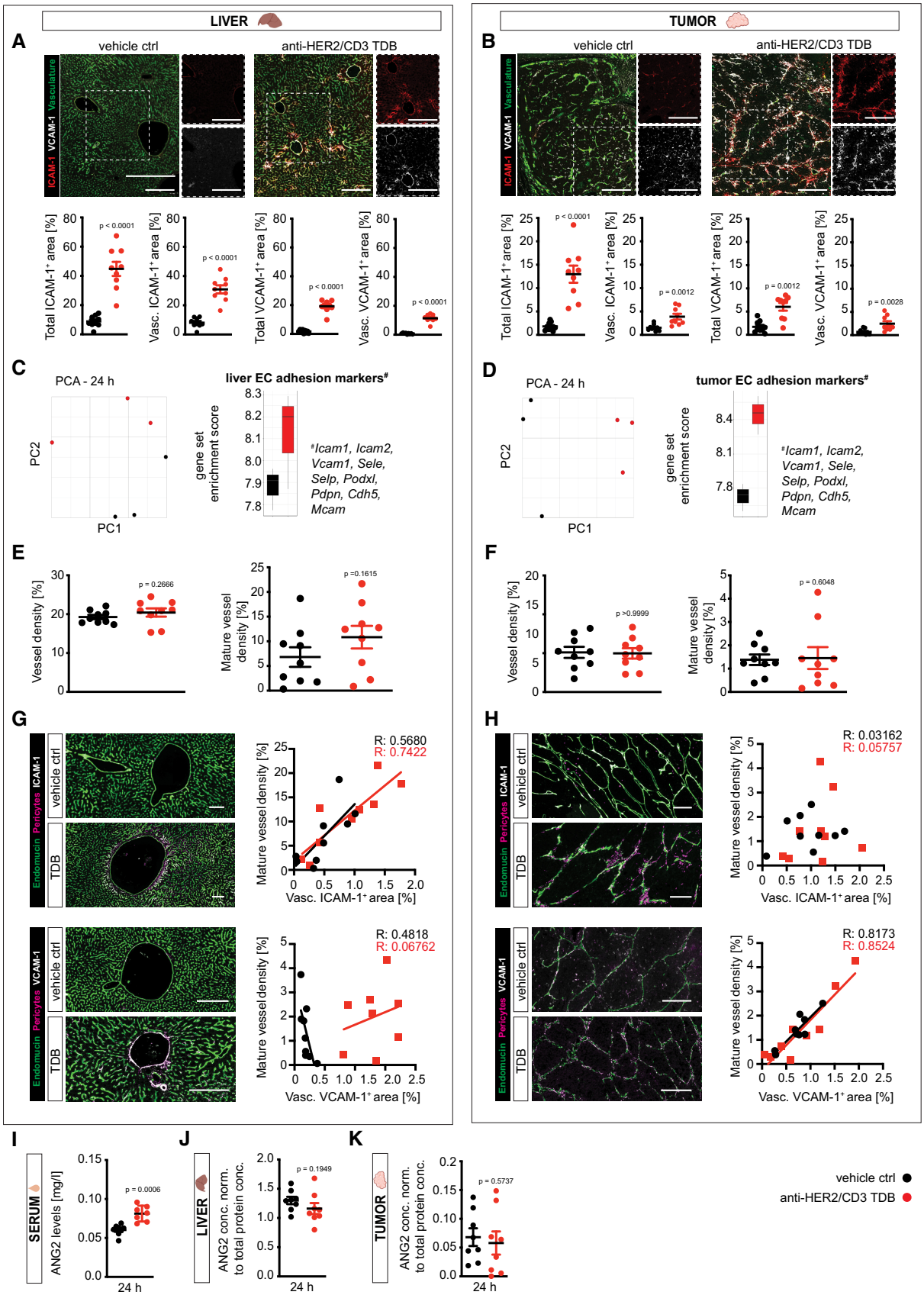

Figure 4.

Figure 4. TDB treatment leads to EC activation and upregulation of adhesion molecules *in vivo*.

A, B Representative images of liver (A) or tumor (B) sections from the Founder5 tumor-bearing mice stained with ICAM-1 (red), VCAM-1 (white), and Endomucin (green) 24 h post treatment. Right panels are enlarged views of the boxed areas showing only ICAM-1 and VCAM-1. Scale bar = 100 μm. Below: quantification of total ICAM-1$^+$ and VCAM-1$^+$ areas as well as vascular (vasc.) ICAM-1$^+$ (ICAM-1$^+$ Endomucin$^+$) and vascular VCAM-1$^+$ (VCAM-1$^+$ Endomucin$^+$) areas normalized to tissue areas. n = 9 mice/treatment.

C, D Principal component analysis (PCA) plots for bulk RNAseq analysis of the liver (n = 3, C) or tumors (n = 3, D) from the Founder5 model 24 h post treatment. Each dot represents a sample and is colored by treatment (left plot). Boxplots (right) show the gene set enrichment score for common adhesion markers in the liver (C) and in the tumor (D) samples. Boxes represent interquartile ranges (IQR), and medians are horizontal lines in the boxes. Whiskers above and below the boxes are the lowest and highest values within 1.5 times IQR.

E, F Densities of total blood vessels (left panel) and mature blood vessels (right panel) in liver (E) and tumor (F) sections from the Founder5 tumor-bearing mice normalized to tissue areas. n = 9 mice/treatment.

G, H Left panels: representative images of liver (G) or tumor (H) sections from the Founder5 model stained with ICAM-1 (white), pericyte markers (pink), and Endomucin (green) (top panel) or stained with VCAM-1 (white), pericyte markers (pink), and Endomucin (green) (bottom panel) 24 h post treatment. Scale bar = 100 μm. Right panels: linear regression analysis comparing adhesion molecule (ICAM-1 and VCAM-1) expression (x-axis) and vessel maturity (y-axis). The coefficients of determination (R) are indicated. n = 9 mice/treatment.

I–K Quantification of circulating (I, n = 7 control-treated and n = 8 anti-HER2/CD3 TDB-treated mice) ANG2 levels as well as tissue ANG2 levels in the liver (J, n = 8 mice/treatment) and tumor (K, n = 8 mice/treatment) 24 h post treatment.

Data information: Black = control-treated mice. Red = anti-HER2/CD3 TDB-treated mice. Mann–Whitney test was run to determine P-values for experiments with two groups unless otherwise indicated. Data are shown as means ± SEM unless otherwise indicated. EC, endothelial cell.
Source data are available online for this figure.

highly expressed in this population. Doublet detection further confirmed this cluster to consist of two distinct cell populations (Figs 5A and EV4B–D).

To better define the impact of TDB treatment on the transcriptional landscape of cells within the liver, we compared gene expression of control- versus TDB-treated samples and saw a systemic response indicated by the dichotomous pattern in the tSNE plots (Fig 5B). Although the number and types of cells captured could be affected by many factors, this pattern was reproduced in several experiments. Furthermore, hepatocytes did not show a significant transcriptional change upon TDB treatment, indicating that the observed changes were due to the TDB treatment and not batch effects.

Given the striking pattern of T cell accumulation around large vessels in the liver, we set out to investigate how different subtypes and/or cell states of liver blood vessels responded to TDB. An in-depth analysis focusing on the 11,757 liver endothelial cells from all samples refined their classification into 12 transcriptional clusters (Fig 5C). To characterize each of these EC clusters, we compared their gene expression profiles to published transcriptional markers of EC subtypes (Kalucka *et al*, 2020a; Data ref: Kalucka *et al*, 2020b). Gratifyingly, we found that our liver ECs matched most closely to the liver ECs in the published dataset (Fig EV4E), and we were able to assign EC subtypes based on expression of several key genes. For example, *Fabp4*, *Vwf*, *Rspo3*, and *Cdh13* were highly expressed in venous ECs, whereas *Flt4*, *Stab2*, and *Lyve-1* were more restricted to sinusoidal endothelium, and the expressions of *Clu*, *Ehd4*, *Plac8*, and *Cd200* were enriched in arteries. The largest subpopulation appears to represent capillary endothelium with high expression for *Bmp2*, *Maf*, and *Dnase1l3* (Fig 5C and D and Dataset EV1). We did not observe any skewed distribution of cells with treatment in any subpopulation. Thus, TDB treatment did not change EC subpopulation identities.

TDB treatment upregulates a transcriptional program that may support T cell adhesion and migration in the large vessels

To gain further insights on how TDB treatment impacted each vascular subtype, we performed differential expression analysis between TDB-treated and control samples within the following four EC subtypes: ECs of large vessels (clusters 7 and 9), small vessels—sinusoidal (clusters 1, 2, 6, 4, 8, and 12), small vessels—capillary (clusters 3, 5, and 10), and the EC/T cell-mixed cluster (cluster 11) (Fig 5E, Dataset EV2). Gene Set Enrichment Analysis (GSEA) using the "hallmark gene sets" from the Molecular Signatures Database (MSigDB) (Subramanian *et al*, 2005; Liberzon *et al*, 2015) revealed that several biological processes, including interferon-inducible inflammatory signaling as well as pro-inflammatory response such as TNFα-mediated signaling, were enriched in TDB-upregulated genes across all EC subtypes (Dataset EV3), indicating a profound

Figure 5. TDB treatment upregulates a transcriptional program that may support T cell adhesion and migration in the large vessels of the liver.

A, B t-SNE plot of 23,736 liver cells (three replicates per treatment) with color-coded clusters and bar graph showing relative transcriptional distribution of various cell types (A) or separated into vehicle control (left, 12,170 cells) and anti-HER2/CD3 TDB-treated (right, 11,566 cells) samples with gray open circles indicating cells belonging to the other treatment group (B). M, myeloid cells.

C UMAP plot color-coded for either transcriptional clusters (left) or treatment (right) of 11,757 liver endothelial cells based on classification shown in (A).

D Heatmap of indicated endothelial cell subtypes showing normalized expression levels of subtype markers among the 12 identified clusters.

E Venn diagram showing significantly upregulated genes when comparing different endothelial cell subtypes. The number of significantly upregulated genes is indicated.

F UMAP plot showing the relative expression levels of genes in "topic 9" from topic modeling. EC clusters 7 and 9 showed highest expression.

G Top 20 DEGs upregulated by TDB in topic 9; the top 11 hits ordered by FDR-adjusted P-values match the DEGs identified in the GSEA analysis in (E).

Source data are available online for this figure.

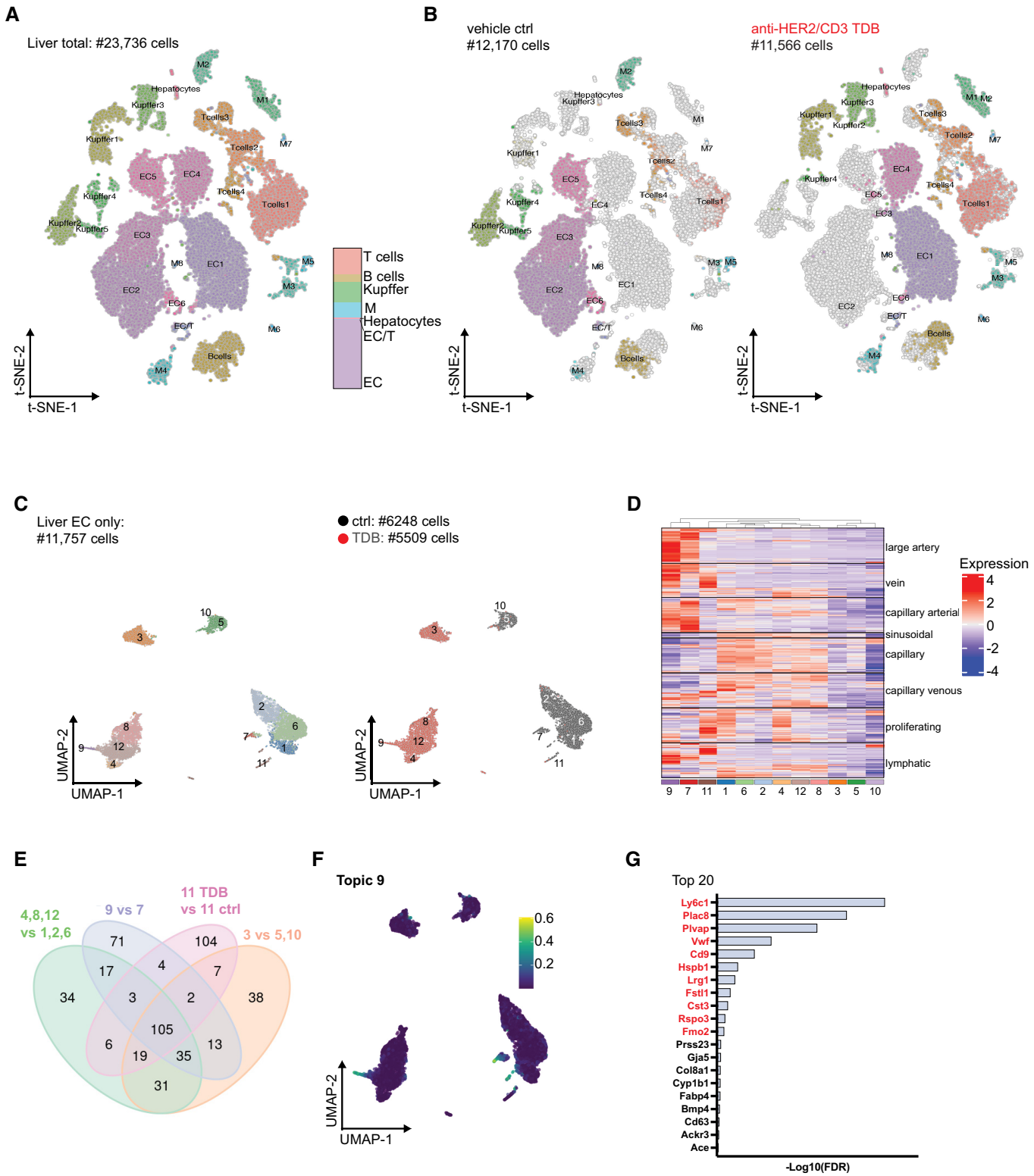

Figure 5.

IFN-licensing response across all liver vessels upon TDB treatment. Such a broad response indicated that it is likely induced by the systemic cytokines and might explain the off-tumor and off-target effect of TDB therapy.

Based on our immunohistochemistry findings, we hypothesized that specific EC subtypes may respond differently to TDB treatment. Beyond the common changes shared by all ECs, we were also able to identify unique biology in individual EC subsets. We identified a

distinct set of 71 genes that were enriched in the ECs of large liver vessels (Fig 5E and Dataset EV4), which might be responsible for increased T cell accumulation in response to TDB treatment. Carrying out GSEA using the Cellular Component list from Gene Ontology (GO C5) of the EC clusters representing large vessels in the control liver (cluster 7, Fig 5C) and TDB-treated liver (cluster 9, Fig 5C), we found that among the top 50 TDB-upregulated hits, 16 gene sets were related to cell adhesion, immune cell activation, cytokine production, and T cell activation. In contrast, using the same analysis on small vessels consisting of capillary or sinusoidal endothelium, only five and six gene sets related to the aforementioned biological functions were upregulated by TDB, respectively (Dataset EV3). These data suggested that TDB upregulates a transcriptional program that may support T cell adhesion and migration in the large vessels to a greater degree than in small vessels.

To deconvolve the functional impact of TDB treatment on ECs using an unbiased approach, we performed topic modeling analysis on the same EC scRNAseq profiles (Dey *et al*, 2017). A model consisting of nine transcriptional programs (topics) was chosen to capture the transcriptional dynamics within the different EC subtypes with and without TDB treatment (Fig EV5A and B). In all EC subtypes, topic 1 scores were enriched in cells under control condition, while topic 5 and topic 6 scores were high in TDB-treated condition, corroborating the previously described IFN-licensing phenotype that was driven by response to TDB in all vessel subtypes (Dataset EV5). Meanwhile topics 2, 3, 4, 8, and 9 explained differences of the EC subtypes regardless of TDB treatment. Topic 7 featured T cell transcriptional profiles, representing the previously identified mixed EC/T cell-mixed cluster. Gratifyingly, topic 9 supported our hypothesis that large vessels responded to TDB more than small vessels. The topic 9 genes were enriched specifically in the large vessels (Figs 5F and EV5B). Among the differentially expressed genes (DEGs) upregulated by TDB in topic 9, we found that the top 11 hits ordered by FDR-adjusted *P*-values matched the DEGs identified in the analysis described above (Fig 5G).

In summary, TDB treatment altered many biological processes involved in vascular responses to inflammatory stimuli independent of EC subtype. In addition, we have identified a specific set of genes that is upregulated in large liver blood vessels that might be responsible for increased T cell accumulation observed upon TDB treatment.

Tetraspanin CD9 is upregulated in large liver blood vessels upon TDB treatment and contributes to T cell–EC adhesion

Among the top 11 DEGs identified by GSEA and topic modeling (Fig 5G) mentioned before, we selected tetraspanin CD9 as an example to demonstrate how we further characterized these candidate factors. *Cd9* expression analysis of the 12 identified transcriptional EC clusters revealed that *Cd9* was already highly expressed at baseline in large liver vessels (Fig 6A, cluster 7) and was further upregulated upon TDB treatment (Fig 6A, cluster 9). *In situ* hybridization and immunofluorescence staining confirmed that the CD9 message and protein localized in the endothelium of large vessels in the liver (Fig 6B and C). In contrast, immunofluorescence staining of tumors revealed that CD9 is mostly expressed by circulating cells within the lumen of blood vessels but not by the endothelium itself (Fig 6D). Flow cytometry analysis of $CD31^+$ liver and tumor ECs showed that CD9-positive ECs are abundant in the liver, whereas a negligible number of CD9-positive ECs are found in the tumor at ~0.5% of live cells (Fig 6E). Primary ECs treated with TDB-conditioned PBMC supernatant also upregulated *Cd9* expression *in vitro*, in line with our scRNAseq data (Fig 6F). To further evaluate our hypothesis that CD9 plays a role in mediating lymphocyte binding upon TDB treatment, we knocked down CD9 in primary ECs and examined T cell adhesion to ECs stimulated by soluble factors released upon TDB-mediated killing. CD9 protein is substantially reduced in primary ECs 48 h after transfection with a CD9-specific siRNA compared to a control siRNA (Fig 6G). When T cell adhesion to primary ECs was evaluated under control condition, no difference between control siRNA and CD9 siRNA was observed (Fig 6H). However, when primary ECs were treated with TDB-conditioned PBMC supernatant, CD9 knockdown modestly reduced the number of T cells attached to the endothelial monolayer. Furthermore, when CD9 knockdown

Figure 6. Tetraspanin CD9 is highly expressed in large liver vessels and upregulated by TDB.

A Box plots showing relative *Cd9* expression levels across the 12 transcriptionally distinct EC clusters defined in Fig 5. Boxes represent interquartile ranges (IQR), and medians are horizontal lines in the boxes. Whiskers above and below the boxes are the lowest and highest values within 1.5 times IQR. Outliers are shown as circle beyond the whiskers. Color codes denote either EC clusters (left) or treatment (right).

B Representative images of an *in situ* hybridization for *Cd9* transcripts distribution in control (upper panels) and TDB-treated (lower panels) liver sections from the Founder5 model. Right panels are enlarged views of the boxed areas highlighting large vessel structures. Scale bar = 1,000 μm.

C, D Representative images of liver (C) or tumor (D) sections from the Founder5 model stained with the following combinations of markers: (left panels) CD9 (green) and ICAM-1 (red); (right panels) CD9 (green) and CD31 (white); 24 h post treatment. In (D) the 3rd right panels are enlarged views of the boxed areas showing $CD9^+$ cells inside the lumen of blood vessels but not in the endothelium; orthogonal views (z) of selected planes are shown on the far right. Scale bar = 100 μm.

E Confirmation of CD9 expression in liver ECs but negligible in tumor ECs. Flow cytometry analysis of CD9 expression on endothelial cells ($CD31^+$) in dissociated livers (top panel) or dissociated tumors (bottom panel) shown as percentage of viable cells, 24 h post treatment (n = 8 mice/treatment). Black = control-treated mice. Red = anti-HER2/CD3 TDB-treated mice. Mann–Whitney test was run to determine *P*-values. Data are shown as mean ± SEM.

F Quantitative RT-qPCR analysis of relative expression of *Cd9* normalized to *Gapdh* in HUVEC after stimulation with either control (blue diamond, n = 9) or PBMC TDB-conditioned supernatant (lilac square, n = 3) for 6 h and 24 h. Ordinary one-way ANOVA was applied. Data are shown as means ± SEM.

G Knockdown efficiency of CD9-specific siRNA was analyzed in HUVEC lysates using the capillary western blot (Wes) assay, and results are shown as gel-like image view (lower panel) and quantification of CD9 band intensity normalized to β-actin (top panel). Two biological experiments (Exp) with two technical replicates per experiment.

H Quantification of T-cell adhesion to a monolayer of HUVECs transfected with either negative control siRNA (black) or CD9-specifc siRNA (green) under shear stress-like conditions (100 rpm) treated with the indicated conditions. All done in biological duplicates with four technical replicates per biological replicate. Representative data of one experiment shown. FOV, field of view. Ordinary one-way ANOVA was applied. Data are shown as means ± SEM.

Source data are available online for this figure.

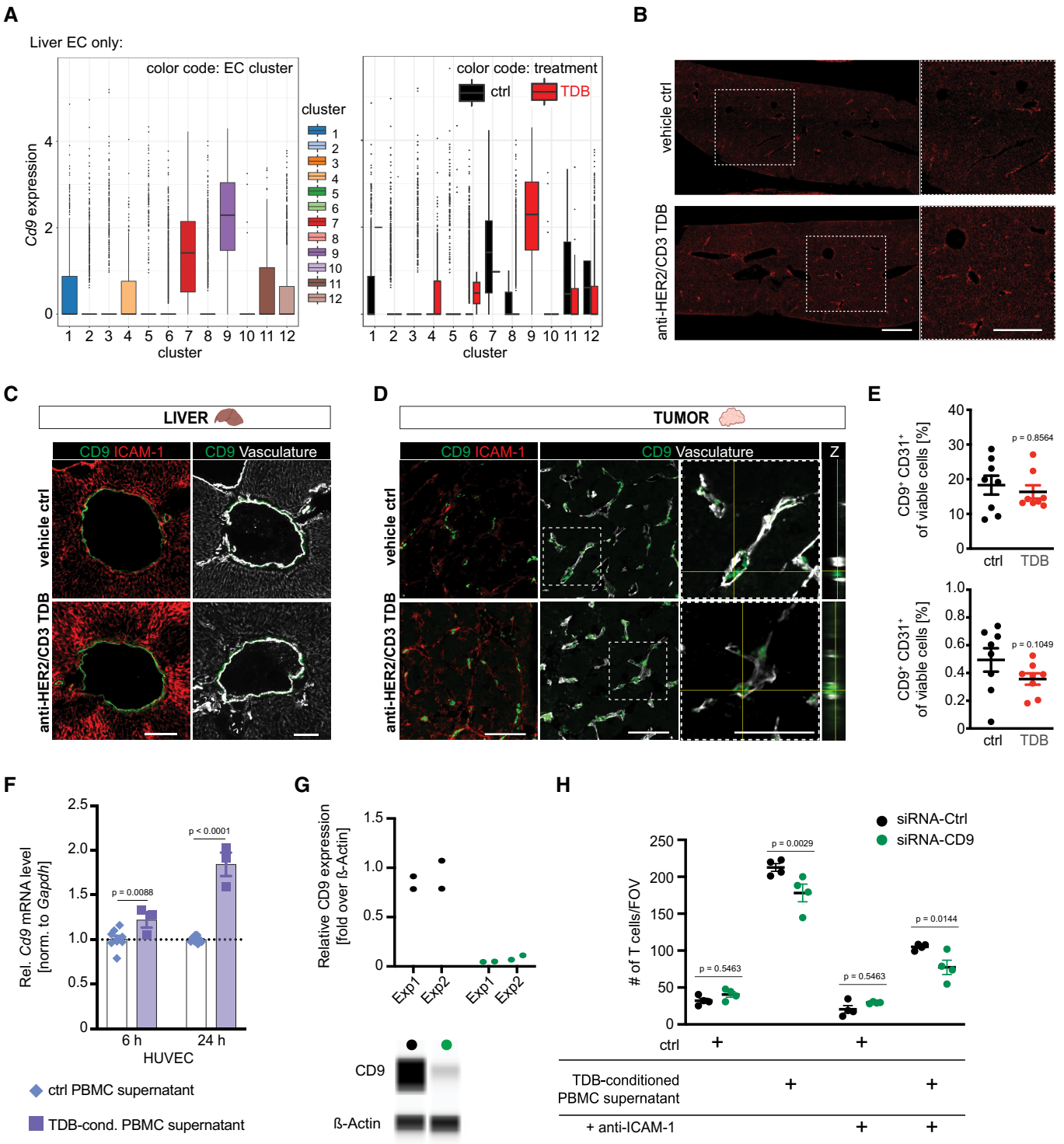

Figure 6.

was combined with ICAM-1 blockade, T cell adhesion was further reduced compared to ICAM-1 blockade alone (Fig 6H), supporting the notion that CD9 enhances T cell adhesion to the endothelium by recruiting ICAM-1 to the EAPs (Barreiro *et al*, 2005, 2008; Bailey *et al*, 2011; Franz *et al*, 2016; Reyes *et al*, 2018).

These findings supported our hypothesis that different factors produced by organ-specific EC subtypes may account for the differential T cell accumulation in normal tissues versus tumors in response to TDB, and CD9 represents one of the candidate factors that mediates enhanced T cell accumulation in the liver. The modest effect of CD9 knockdown implies that multiple factors may be required to account for the observed phenotype *in vivo*.

Taken together, our data provided new insights on how different vascular subtypes respond to cancer immunotherapy and could

provide novel opportunities to improve the safety and/or efficacy of this class of cancer therapies.

Discussion

Over the past decade, tremendous progress has been made in enhancing our understanding of the complex mechanisms and pathways that regulate the immune system's response to cancer. Innovative approaches have been employed to leverage the antitumor immune response, leading to therapeutic advances in the field of cancer immunotherapy (CIT). However, despite the remarkable achievements, a large number of patients are not yet benefiting from these therapies. Some of the underlying reasons and challenges have been extensively described elsewhere (Ventola, 2017a, 2017b; Hegde & Chen, 2020), many of which reflect the complex and highly regulated nature of the immune system. In this study, we aimed at improving our understanding of the impact of TDB as an emerging modality in CIT, and we focused on T cell trafficking and its tissue distribution with the ultimate goal of increasing T cell infiltration into tumors and/or reducing their redistribution into normal organs. More specifically, we wanted to determine if and how different subtypes of blood vessels support T cell redistribution in response to TDB because the endothelium is an important gateway for T cell trafficking.

Defying conventional wisdom, we found that TDB treatment leads to a more profound acute accumulation of T cells in the liver compared to tumors. Based on the spatial and temporal pattern of the T cell accumulation, we hypothesize that organ-specific ECs may account for the differential T cell accumulation in normal tissues versus tumors in response to TDB, and we set out to identify the responsible EC molecular phenotype using single-cell analyses. Previous scRNAseq studies of various tumor types have revealed an extensive heterogeneity in tumor cells and tumor-associated stromal cell types, including ECs, fibroblasts, smooth muscle cells, and immune cells (Patel *et al*, 2014; Lambrechts *et al*, 2018; Zhao *et al*, 2018). It is hypothesized that the extent of heterogeneity is shaped by interactions with other cells in the tumor mass, but could also be affected by various factors such as therapies. Therefore, we wondered whether TDB treatment leads to a transcriptionally heterogenous response and whether this goes beyond the tumor and its microenvironment and could potentially explain the off-tumor effects of TDB.

To the best of our knowledge, this study is the first in-depth transcriptional analysis of how ECs of normal organs respond to a cancer immunotherapy agent, in this case TDB. We found that TDB treatment induced dramatic transcriptional changes in liver ECs. Previous studies characterizing the impact of immune checkpoint inhibitor therapy (another modality of CIT) together with TGFβ blockade on the tumor microenvironment have found that all major cell types throughout the tumor microenvironment showed a unique transcriptional response referred to as IFN licensing as these were highly enriched for a broad range of molecules associated with interferon signaling (Grauel *et al*, 2020). Similarly, we also observed a TDB-mediated IFN response signature in the liver. These findings suggest that enhancing T cell activities within tumors can lead to IFN release and invoke broad transcriptional changes in many normal cell types irrespective of the CIT modalities. In addition to the IFN-licensing program, we also found that TDB treatment led to unique transcriptional responses depending on EC subtype. In this regard, we identified a specific subset of genes highly enriched in ECs of large vessels. Within this gene set, we identified tetraspanin CD9 as one of the potential contributors that facilitate T cell adhesion to the large liver vessels in response to TDB. Previous studies have shown that CD9 is a component of the EAPs, a molecular complex that promotes firm leukocyte attachment to the endothelium and increases the probability of leukocyte trans-endothelial migration (Barreiro *et al*, 2008; Bailey *et al*, 2011; Franz *et al*, 2016; Reyes *et al*, 2018). Knockdown of CD9 in primary endothelial cells dampened the lymphocyte–endothelium adhesion in response to factors released from TDB-mediated killing of target cells (Fig 6H), substantiating our hypothesis that CD9 also functions in the context of response to TDB. Our *in vitro* functional assay demonstrated that CD9 alone plays a modest role in supporting T cell–EC interaction, and it contributes to the adhesive function of ICAM-1. These results indicate that multiple factors are likely acting in concert instead of alone to promote T cell infiltration into normal organs. Therefore, a systematic evaluation of multiple candidate factors individually and in combination is required to identify optimal targets for the management of TDB treatment.

Many current efforts focus on how targeting other cell types in combination with CIT could improve CIT efficacy and/or safety (Arora & Pal, 2021). Our study indicated that the vasculature could be a promising target. Over the past decades, vascular modulating agents have been shown to have the potential to modulate the tumor microenvironment and improve CIT activity (Fukumura *et al*, 2018; Ciciola *et al*, 2020; Lee *et al*, 2020). Our findings suggest that modulating the vasculature in normal tissues may also have the potential to improve the safety and efficacy profile of TDB, which could ultimately lead to better patient outcomes. We hypothesize that reducing leukocyte–endothelial interactions in tumor-antigen-negative organs may limit the extravasation of T cells into normal tissues, thereof alleviating off-tumor adverse response. In addition, shunting T cells away from normal organs might increase the pool of T cells that could be recruited into tumors, leading to improved antitumor efficacy.

Given these exciting new findings, we would also like to point out the limitations of this study. First, the model systems used are not of human origin, and translating such findings into human patients is a common challenge many biomedical studies are facing. One factor that alleviates this concern is that many common features are shared between our model system and findings in human patients, including acute cytokine release and lymphocyte margination induced by TDB. Directly validating T cell redistribution in human patients is currently impractical, given the ethical challenges of taking biopsies from normal organs from cancer patients. The ultimate proof of our finding in human awaits major technical advances. Second, the response to TDB is a multistep complex process, and our work is part of the collective efforts to clearly define this process.

Taking our data and published studies together, we propose that TDB-mediated T cell activation is the first step that triggers the release of cytokines and chemokines, which in turn induces vascular activation in normal tissues, including the liver. This leads to subsequent infiltration of T cells to the liver and promotes hepatic injury.

However, we cannot exclude the possibility that circulating tumor cells might enter the liver, and that some hepatocytes are pre-conditioned by making contact with a tumor cell under the influence of the TDB.

Despite the limitation, our data highlight the importance of carefully characterizing the role of the vasculature in CIT and opens a new area of investigation and innovation to improve the safety and efficacy profiles of CIT.

Materials and Methods

Reagents and Tools table

Reagent/resource	Reference or source	Identifier or catalog number
Experimental models		
HUVEC-c, single donor, female, Caucasian, LOT#434Z011	Promocell	C-12200
FVB/NJ mice	Jackson Laboratory	JAX stock number: 001800
hu.CD3E.tg.B6N mice	Charles River Labs	#6679
Recombinant DNA		
Not applicable		
Antibodies		
Fixable Viability Dye eFluor™ 780	ThermoFisher Scientific	65-0865-14
Purified Rat Anti-Mouse CD16/CD32 (Mouse BD Fc Block™), clone 2.4G2 (RUO)	BD Biosciences	553141
FcR Blocking Reagent, human	Miltenyi Biotec	130-059-901
Mouse anti-human CD54-BV421, clone HA58	BD Biosciences	566262
Mouse anti-human CD106-FITC, clone 51-10C9	BD Biosciences	551146
Rat anti-mouse CD4-BV650, clone GK1.5 (RUO)	BD Biosciences	563232
Rat anti-mouse CD4-PE/Cyanine7, clone RM4-5	Biolegend	100528
Rat anti-mouse CD45-BUV395, clone 30-F11 (RUO)	BD Biosciences	564279
Rat anti-mouse CD8a-BV711, clone 53-6.7 (RUO)	BD Biosciences	563046
Rat anti-mouse CD8a-BUV737, clone 5H10-1 (RUO)	BD Biosciences	752639
Rat anti-mouse Ki-67 eFluor™ 450, clone SolA15	ThermoFisher Scientific	48-5698-82
Armenian Hamster anti-mouse CD69-BV650, clone H1.2F3 (RUO)	Biolegend	104541
Mouse anti-human GZMB-APC, clone GB12	ThermoFisher Scientific	MHGB05
Rat anti-mouse CD44-BV510, clone IM7 (RUO)	BD Biosciences	563114
Rat anti-mouse CD62L-FITC, clone MEL-14 (RUO)	BD Biosciences	553150
Rat anti-mouse CD31-Alexa Fluor® 488, clone 390 (RUO)	BD Biosciences	563607
Rat anti-mouse CD9-eFluor™ 450, clone KMC8	ThermoFisher Scientific	48-0091-82
CD8a:10126 [21E3.TRANS]	This paper	Not applicable
Pan Cytokeratin [AE1/AE3]	Abcam	Ab27988
Rat monoclonal anti-Endomucin [V.7C7.1]	Abcam	ab106100
Rabbit monoclonal anti-VCAM-1 [EPR5047]	Abcam	ab215380
Rat monoclonal anti-ICAM-1 [YN1/1.7.4]	Abcam	ab119871
Rabbit monoclonal anti-CD3 [SP7]	ThermoFisher Scientific	RM-9107-S
Rabbit polyclonal anti-Desmin	Abcam	ab15200
Rabbit polyclonal anti-NG2	Sigma-Aldrich	AB5320
Rabbit polyclonal anti-Smooth Muscle Actin	ThermoFisher Scientific	RB9010P
Anti-CD9 antibody produced in rabbit	Sigma-Aldrich	C9993
Monoclonal rat Anti-Mouse Panendothelial Cell Antigen, MECA-32	BD Pharmingen™	553849
Donkey anti-rabbit IgG Alexa Fluor® 594	ThermoFisher Scientific	A-21207
Donkey anti-rat IgG Alexa Fluor® 647	Jackson ImmunoResearch	712-605-153

Reagents and Tools table (continued)

Reagent/resource	Reference or source	Identifier or catalog number
RNAscope® Probe- Mm-Cd9-C1	Advanced Cell Diagnostics, Inc.	430631
Human ICAM-1/CD54	R&D systems	AF720
b-Actin (D6A8) rabbit mAb	Cell Signaling Technology	8457
Rabbit polyclonal anti-CD9 antibody	Abcam	ab223052
Anti-CD20/CD3 TDB	This paper	2H7v/6/38E4.v.1
Anti-HER2(4D5-2C11)/CD3 used concentrations for the antibodies can be found in Materials and Methods	This paper	PUR# 1BE46637
Oligonucleotides and sequence-based reagents		
Silencer™ Negative control No. 2 siRNA	ThermoFisher Scientific	AM4613
Silencer® Select Cd9 ID:s2599	ThermoFisher Scientific	4392420
Chemicals, enzymes and other reagents		
cOmplete™, Mini, EDTA-free Protease Inhibitor Cocktail	Roche	4693159001
Software		
R version 4.0.0 (2020-04-24)	R Core Team (2020)	https://www.R-project.org/
Definiens Developer XD	Baatz *et al* (2009), Definiens	Definiens.com
Matlab, r2020b	Mathworks	https://www.mathworks.com/
10x Genomics Cell Ranger 3.1.0	Zheng *et al* (2017), 10x Genomics	10xgenomics.com
BioRender.com	BioRender.com	BioRender.com
Other		
MILLIPLEX MAP Human Cytokine/Chemokine Magnetic Bead Panel – Premixed 30 Plex – Immunology Multiplex Assay	Millipore	HCYTMAG-60K-PX30
MILLIPLEX MAP Mouse Cytokine/Chemokine Magnetic Bead Panel – Premixed 32 Plex – Immunology Multiplex Assay	Millipore	MCYTMAG-70K-PX32
Pan T Cell Isolation Kit, human	Miltenyi Biotec	130-096-535
Mouse/Rat Angiopoietin-2 Quantikine ELISA Kit	R&D Systems	MANG20
Mouse Angiopoietin-2 ELISA Kit	Abcam	ab171335
FOXP3 Fix/Perm Buffer Set	421403	Biolegend
Alexa Fluor™ 488 Tyramide SuperBoost™	Invitrogen	B40932
TSA Cyanine 5	Akoya Bioscience Inc.	NEL745001KT
RNAscope® Multiplex Fluorescent Detection Kit v2	Advanced Cell Diagnostics, Inc.	323110
Liver Dissociation Kit, mouse	Miltenyi Biotec	130-105-807
Agilent High Sensitivity DNA Kit	Agilent	5067-4626
Kapa Library Quantification Kit	Kapa Biosystems	KK4873
RNAeasy Plus Mini Kit (50)	Qiagen	74134
P5 Primary Cell Amaxa™ 4D-Nucleofector Kit	Lonza	V4XP-5024
12–230 kDa Separation Module, 25 capillary cartridges	ProteinSimple	SM-W004
Anti-rabbit detection module	ProteinSimple	DM-001
Pierce™ BCA Assay Kit	ThermoFisher Scientific	23227
High-Capacity RNA-to-cDNA™ Kit	ThermoFisher Scientific	4388950
TaqMan™ Fast Advanced Master Mix	ThermoFisher Scientific	444964
Human Cd9 TaqMan® Gene expression assay	ThermoFisher Scientific	Hs01124022_m1
Human Gapdh TaqMan® Gene expression assay	ThermoFisher Scientific	4333764F
Corning Matrigel Matrix	Corning	356237

Methods and Protocols

Generation of TDB-conditioned PBMC supernatant and T cell adhesion assays

Peripheral blood mononuclear cells (PBMCs) were isolated from whole blood of healthy donors by Ficoll separation using Lymphocyte Separation Medium (LSM™, ref: 0850494-CF, MP Biomedicals). PBMCs were treated with 0.5 μg/ml anti-CD20/CD3 TDB (2H7v/6/38E4.v.1) and cultured over night at 37°C, 5% CO_2 in endothelial cell growth medium-2 (EGM™-2 Endothelial Cell Growth Medium-2 BulletKit™, ref: CC-3162, LONZA). B cell killing was confirmed by flow cytometric analysis. Supernatants from untreated PBMCs as well as TDB-conditioned PBMCs were used for further downstream analysis, e.g., cytokine analysis, EC activation assay, and T cell adhesion assay.

Endothelial cell culture

Primary endothelial cells (HUVEC-c, single donor, female, Caucasian, Promocell, ref: C-12200, Lot# 434Z011) were cultured in endothelial cell growth medium-2 (EGM™-2 Endothelial Cell Growth Medium-2 BulletKit™, ref: CC-3162, LONZA) at 37°C, 5% CO_2 until they reached 90–95% confluency. HUVECs at passage 5 were used in this study.

Endothelial cell activation assay in vitro

Confluent endothelial cells were incubated with TDB-conditioned PBMC supernatant for 6 h at 37°C, 5% CO_2. Supernatants were harvested and cytokine analysis was performed. Cells were harvested using TrypLE™ (ThermoFisher Scientific, ref: 12604013), and single-cell suspensions were incubated 15 min at room temperature in the dark with the fixable viability dye (ref: 65-0865-14, ThermoFisher Scientific). After washing with FACS buffer, cells were blocked with anti-human FcR blocking reagent (Miltenyi Biotec, ref: 130-059-901). After blocking, cells were incubated with either mouse anti-human CD54-BV421 (BD Biosciences, ref: 566262, clone HA58) or mouse anti-human CD106-FITC (BD Biosciences, ref: 551146, clone 51-10C9). After wash, samples were fixed and run on analyzers.

Human cytokine and chemokine analysis

Cytokines and chemokines from TDB-conditioned PBMC supernatant were analyzed using the human cytokine Luminex assay (HCYTMAG-60K-PX30, Millipore) according to the manufacturer's instructions.

T cell adhesion assay in vitro

Human Pan T cells were isolated from PBMCs of whole blood of healthy donors using a human Pan T cell isolation kit (Miltenyi Biotec, ref: 130-096-535) according to the manufacturer's instructions. Cells were cultured in ImmunoCult™-XF T Cell Expansion medium (STEMCELL Technologies, ref: 10981) at 37°C, 5% CO_2. Primary endothelial cells (HUVEC-c, single donor, female, Caucasian, Promocell, ref: C-12200, Lot# 434Z011) were cultured in endothelial cell growth medium-2 (EGM™-2 Endothelial Cell Growth Medium-2 BulletKit™, ref: CC-3162, LONZA) at 37°C, 5% CO_2 until they reached 90–95% confluency in 96-well plates. Subsequently, endothelial cells were incubated with TDB-conditioned PBMC supernatant for 24 h at 37°C, 5% CO_2. Prior to performing T cell adhesion assay, T cells were labeled using CellTracker™ Green CMFDA Dye (ThermoFisher Scientific, ref: C7025; final concentration of 0.5 μM) in endothelial cell medium. For T cell adhesion assay, 7500 labeled T cells per well were added to TDB-conditioned PBMC supernatant-treated endothelial cells and centrifuged for 3 min, RT at 300 rpm. Images (=T_1) of every well were acquired using Incucyte® Zoom (Essen BioScience). Subsequently, plates were inverted and centrifuged for 15 s at 30 *g*. Images of every well (=T_2) were acquired using Incucyte® Zoom (Essen BioScience). Percentage of adhesion was calculated as: [remaining cells (T_2)/starting cells (T_1) × 100].

Endothelial cell transfection

Primary endothelial cells (HUVEC-c, single donor, female, Caucasian, Promocell, ref: C-12200, Lot# 434Z011) were cultured in endothelial cell growth medium-2 (EGM™-2 Endothelial Cell Growth Medium-2 BulletKit™, ref: CC-3162, LONZA) at 37°C, 5% CO_2 until they reached 90–95% confluency. For knockdown of CD9, a siRNA specific for CD9 (Silencer® Select Cd9 ID:s2599, ThermoFisher Scientific, ref: 4392420) was used. As control siRNA, a non-targeting siRNA (Silencer™ Negative control No. 2 siRNA, ThermoFisher Scientific, ref: AM4613) was used. Per transfection 2×10^6 HUVEC cells were transfected with 200 pmol of siRNAs using the P5 Primary Cell 4D-Nucleofector™ X Kit L (Lonza, ref: V4XP-5024) according to the manufacturer's instructions. After 48 h, knockdown efficacy was assessed and functional T cell adhesion assays were performed.

Functional T cell adhesion assay after CD9 knockdown

Human Pan T cells were isolated from PBMCs of whole blood of healthy donors using a human Pan T cell isolation kit (Miltenyi Biotec, ref: 130-096-535) according to the manufacturer's instructions. Cells were cultured in ImmunoCult™-XF T Cell Expansion medium (STEMCELL Technologies, ref: 10981) supplemented with 10 ng/ml rh-IL2 (Roche, ref: 11147528001) for 24 h. Next day, T cells were stimulated for 3 days with ImmunoCult™-XF T Cell Expansion medium (STEMCELL Technologies, ref: 10981) supplemented with 10 ng/ml rh-IL2 (Roche, ref: 11147528001) and ImmunoCult™-Human CD3/CD28 T cell Activator (STEMCELL Technologies, ref: 10971). Prior to performing T cell adhesion assay, T cells were labeled using CellTracker™ Green CMFDA Dye (ThermoFisher Scientific, ref: C7025; final concentration of 0.5 μM) in endothelial cell medium.

HUVECs transfected with either negative control siRNA or siRNA specific for CD9 were incubated either in control medium or with TDB-conditioned PBMC supernatant with and without 12.5 μg/ml anti-ICAM-1 (R&D systems, ref: AF720) for 24 h at 37°C, 5% CO_2.

For T cell adhesion assay, 44,500 labeled T cells per well (24-well plates) were added to the endothelial cells while shaking (100 rpm) for 10 min to mimic shear stress-like conditions. Subsequently, medium was aspirated and replaced with endothelial growth medium. Images of every well were acquired using Incucyte® Zoom (Essen BioScience).

Western blot using Simple Western™

Forty-eight hours post transfection, HUVECs were lysed in Triton X-100-containing lysis buffer (50 nM Tris HCl, pH 7.4, 1% [vol/vol] Triton X-100, 150 mM NaCl, protease inhibitors (cOmplete™, Mini, EDTA-free Protease Inhibitor Cocktail, Roche, ref:

04693159001)) for 30 min on ice and then centrifuged at 4°C. Total protein concentrations were determined using the Pierce Micro BCA Protein Assay Kit (ThermoFisher Scientific, ref: 23227). A capillary-based western blotting system (ProteinSimple Wes, ref: SM-W004) was used to assess protein expression. All procedures were completed according to the manufacturer's instructions and default settings. Protein lysate concentration used was 4 mg/ml. CD9 knockdown efficacy was analyzed using polyclonal rabbit anti-CD9 (1:20, Abcam, ref: ab223052). β-Actin (D6A8) (rabbit mAb, 1:20, Cell Signaling Technology, ref: 8457) was used for normalization. The anti-rabbit secondary antibodies included in the Wes Detection Module kit (ProteinSimple Wes, ref: DM-001) were used. All data were analyzed with the Compass Software associated with the Wes instrument (ProteinSimple Wes).

Real-time quantitative PCR

Total RNA was extracted from cells with Rneasy Mini Plus Kits (ref: 74034, Qiagen) and reverse-transcribed with High-Capacity RNA-to-cDNA™ Kit (ref: 4388950, ThermoFisher Scientific) following manufacturer's instructions. The PCR reactions were set up by mixing cDNA template with primers and TaqMan™ Fast Advanced Master Mix (ref: 444964, ThermoFisher Scientific) according to manufacturer's protocol. Gene expression was measured on a ViiA™ 7 Real-Time PCR System (Applied Biosystems): Human *Cd9* TaqMan® Gene expression assay: Hs01124022_m1 (ThermoFisher Scientific) and human *Gapdh* TaqMan® Gene expression assay: 4333764F (ThermoFisher Scientific).

Animals

All *in vivo* mouse experimental procedures conformed to the guiding principles of the American Physiology Society and were approved by the Institutional Animal Care and Use Committee (IACUC) at Genentech, Inc. All mice used in our experiments were between 6 and 12 weeks of age and were housed under standard housing conditions at the animal research facility (Genentech Inc.). In order to avoid biases related to sex differences in the immune system and tumor growth, only female mice were used in this study if not stated otherwise. Female and male FVB/NJ (JAX:001800) mice between 6 and 8 weeks of age were purchased from Jackson Laboratory. Female hu.CD3E.tg.B6N (#6679) mice between 6 and 8 weeks of age were purchased from Charles River Labs. Animals were age- and sex-matched and randomly assigned in control and treatment groups. Mice were maintained on a standard day–night (12-h) cycle, with *ad libitum* access to food (standard chow) and water.

Fo5 tumor allograft model (as described in Li et al, 2018)

A 1-cm incision was made in the skin just rostral to the third mammary fat pad on FVB WT mice obtained from Jackson Laboratory (FVB/NJ JAX stock number: 001800). A pocket for the tumor was made into the no. 2/3 mammary fat pad and a 2 × 2 mm MMTV-HER2-transgenic Founder #5 (Fo5) tumor section was placed into the pocket (Lewis Phillips *et al*, 2008). The skin was closed using wound clips. Wound clips were removed at 7–10 days post-surgery, and mice were monitored for appearance of palpable tumors. When tumor volumes grew to an average of approximately 350–500 mm^3, they were randomly placed into treatment cohorts with an equivalent tumor volume average size. Only animals that appeared to be healthy and free of obvious abnormalities were used in the study.

For efficacy study shown in Fig 1A, dosing initiated (day 0) and mice were treated as indicated. All treatments were administered QWx5, intravenously, by tail vein injection at a volume of 0.1 ml on days 0, 7, 14, 21, and 28. Tumor volumes and weights were measured at least two times a week for the duration of the study. The study ended on day 31 after first treatment.

For acute response studies, anti-HER2(4D5-2C11)/CD3 antibody diluted in vehicle solution (20 mM Histidine acetate, 240 mM sucrose, 0.02%Tween-20, pH 5.5 buffer) was administered once to mice intravenously (i.v.) by tail vein injection or intraperitoneally (i.p.) at 5 mg/kg (if not stated otherwise). The vehicle buffer was used as the control and was given at the same volume as the treatment antibodies. Mice were harvested 24 h or 4 days post treatment.

ID8/LYPD1X4 ovarian cancer model (as described in Lo et al, 2021)

Four million ID8-LYPD1 cells/mouse suspended in HBSS/Matrigel (ref: 356237, Corning) were inoculated in the thoracic mammary fat pad (0.2 ml) of female hu.CD3E.tg.B6N mice (Charles River Labs stock number: 6679). Mice with 150–250 mm^3 tumor volume were treatment randomized, and dosing was initiated (day 0). Only animals that appeared to be healthy and free of obvious abnormalities were used in the study. For acute response studies, anti-LYPD1/CD3 antibody diluted in vehicle solution (20 mM Histidine acetate, 240 mM sucrose, 0.02%Tween-20, pH 5.5 buffer) was administered once to mice intravenously (i.v.) by tail vein injection at 10 mg/kg. The vehicle buffer was used as the control, and was given at the same volume as the treatment antibodies. Mice were harvested 24 h or 4 days post treatment.

Blinding and randomization statement

The experimenter was not blinded when sacrificing animals for an experiment. Animals were randomly placed into treatment cohorts with an equivalent tumor volume average size. The experimenter was blinded when processing samples for analysis, during data acquisition, and data analysis.

Bispecific antibodies

Bispecific antibodies were produced as described earlier (Junttila *et al*, 2014; Sun *et al*, 2015; Li *et al*, 2019; Lo *et al*, 2021).

Mouse serum cytokine and chemokine analysis

Mouse blood was transferred to a serum separator tubes (ref: 365967, BD Biosciences) and centrifuged at 15,000 *g* for 10 min at room temperature (RT). Cytokines and chemokines from mouse serum were analyzed using the mouse cytokine Luminex assay (MCYTMG-70K-PX32, Millipore) according to the manufacturer's instructions.

Quantification of mouse serum ANG2 protein levels by ELISA

Mouse blood was transferred to a serum separator tubes (ref: 365967, BD Biosciences) and centrifuged at 15,000 *g* for 10 min at room temperature (RT). Quantification of mouse ANG2 protein levels from mouse serum was analyzed according to the manufacturer's instructions (R&D Systems, Quantikine MANG20).

Mouse tissue cytokine and chemokine analysis

Liver and tumor tissue were snap-frozen in 500 μl tissue lysis buffer (1× protease inhibitor cocktail) per 100 mg tissue. Liver and tumor

tissues were cut into smaller pieces with scissors and transferred into Soft Tissue Homogenizing bead tubes (ref: 10158-610, VWR) or Lysing Matrix D tube (ref: 116913050, MP), respectively. Tissue samples were homogenized using Bead Ruptor Elite—Omni Inc. (6.8 m/s, 30 s, 1 cycle). Samples were kept on ice for 10 min and then centrifuged at 20,000 *g* for 10 min at 4°C. Supernatants were filtered through ultrafree-MC centrifugal filter (0.45 μm; ref: UFC30HVNB, Millipore). Total protein concentration of clear homogenate was determined by Pierce Micro BCA Protein Assay Kit (ThermoFisher Scientific, ref: 23227). Total protein concentration was normalized to tissue weight. Cytokines and chemokines from tissue homogenates were analyzed using the mouse cytokine Luminex assay (MCYTMG-70K-PX32, Millipore) according to the manufacturer's instructions.

Quantification of mouse tissue ANG2 protein levels by ELISA

Quantification of mouse ANG2 protein levels from tissue homogenates (see above) was analyzed according to the manufacturer's instructions (ref: ab171335, Abcam). ANG2 levels were normalized to total protein concentration.

Mouse blood preparation for flow cytometry analysis

Mouse peripheral blood was collected in tubes containing EDTA (ref: 41.1504.105, Sarstedt Inc.). Red blood cells were lysed using ACK lysis buffer once to twice. Remaining cells were resuspended in FACS buffer. Small aliquots were taken for cell counting. The rest of the samples were stained with the indicated markers for flow cytometry analysis. The live/dead fixable near-infrared dye (ref: 65-0865-14, ThermoFisher Scientific) was used to exclude dead cells.

Mouse tumor tissue preparation for flow cytometry analysis

Tumors were cut into small pieces of 2–4 mm and transferred to gentleMACS C Tubes (ref: 130096334, Miltenyi Biotec) in 5 ml of CDTI buffer (RPMI supplemented with 2% heat-inactivated FBS, 2 mg/ml collagenase D [ref: 11088882001, Roche], 40 U/ml DNase bovine pancreas grade I [ref: D4527-40 KU, SIGMA-Aldrich], and 1 mg/ml trypsin inhibitor [ref: T9003-1G, Sigma-Aldrich]). C-tubes were placed onto gentleMACS Octo Dissociator, and GentleMACS program m_impTumor_03 was used, followed by 45-min incubation at 37°C and GentleMACS program m_impTumor_01. After centrifugation (1,400 rpm, 7 min, 4°C), red blood cells were lysed using ACK lysis buffer. Samples were filtered through a 100-μm cell strainer and spun down at 1,500 rpm for 7 min. Single-cell suspensions were prepared in FACS buffer and stained against the indicated markers for flow cytometric analysis. The live/dead fixable near-infrared dye (ref: 65-0865-14, ThermoFisher Scientific) was used to exclude dead cells.

Mouse liver tissue preparation for flow cytometry analysis

Livers were cut into small pieces of 2–4 mm and transferred to 6-well plates containing 5 ml of 2 mg/ml collagenase D (ref: 11088866001, Roche) solution. Liver tissues were incubated at 37°C for 40 min and filtered through a 70-μm cell strainer. After centrifugation (1,500 rpm, 5 min, 4°C), red blood cells were lysed using ACK lysis buffer. Samples were spun down at 1,500 rpm for 5 min, and single-cell suspensions were prepared in FACS buffer and stained against the indicated markers for flow cytometric analysis. The live/dead fixable near-infrared dye (ref: 65-0865-14, ThermoFisher Scientific) was used to exclude dead cells.

Flow cytometry analysis

Single-cell suspensions were incubated 15 min at room temperature in the dark with the fixable viability dye (ref: 65-0865-14, ThermoFisher Scientific) and washed with FACS buffer and blocked with anti-mouse CD16/CD32 (ref: 553141, BD Fc Block™). After blocking, cells were incubated with conjugated antibodies. After wash, samples were either fixed and permeabilized (ref: 421403, Biolegend) for intracellular staining or fixed and run on analyzers.

Antibodies used in the flow cytometric analyses are listed in the Reagents and Tools table.

Hematoxylin and eosin (H&E) staining

Six-micrometer thick formalin-fixed paraffin-embedded unstained slides were stained for H&Es using standard protocols.

panCK/CD8 IHC dual staining

Immunohistochemistry (IHC) was performed on 4-μm thick formalin-fixed paraffin-embedded tissue sections mounted on glass slides. All IHC steps were carried out on the Ventana Discovery Ultra (Ventana Medical Systems, Tucson, AZ) autostainer. Pretreatment was done with Cell Conditioning Solution 1 for 64 min. Primary antibody CD8a (Genentech Inc., South San Francisco, CA) was used at the concentration of 5 μg/ml and was incubated on slides for 60 min at 37°C. Ventana Rabbit OmniMap (Ventana Medical Systems, AZ) was used as the detection system and incubated for 16 min followed by Ventana DAB. Elution was performed with Cell Conditioning Solution 2 followed by the primary antibody Pan Cytokeratin (ab27988, Abcam, Cambridge, MA) at 2 μg/ml for 32 min at 37°C. A rabbit recombinant anti-IgG1+IgG2a+IgG2 antibody (Abcam, Cambridge, MA) was used at 5 μg/ml for 32 min. Ventana Rabbit OmniMap (Ventana Medical Systems, AZ) was used as the detection system and incubated for 16 min. Ventana Discovery Purple and Hematoxylin II were used for chromogenic detection and counterstain. Slides were scanned on a NanoZoomer X360 whole slide imager (Hamamatsu, Bridgewater, NJ) at 200× final magnification.

Immunofluorescence staining (IF)

Formalin-fixed paraffin-embedded tumor and liver samples were used (thickness: 6 μm). For IF, slides were de-paraffinized in xylenes, re-hydrated, and boiled in Dako target retrieval buffer, pH 6 (ref: S2369, Dako) for 25 min. Samples were first blocked with Avidin/Biotin (ref: SP-2001, Vector) following manufacturer's instructions and then for 60 min at room temperature with Dako protein-free blocking solution (ref: X0909, Dako). Primary antibody for endomucin (rat monoclonal [V.7c7.1], Abcam ab106100—1:100) was applied in Dako protein-free blocking solution overnight at 4°C, followed by a 2-min Alexa 488-tyramide labeling reaction following the manufacturer's instructions (Alexa Fluor™ 488 Tyramide SuperBoost™; Invitrogen B40932). Subsequently, samples were subjected to a second antigen retrieval (as above), then blocked with Dako protein-free blocking solution (ref: X0909, Dako) for 60 min at room temperature before applying the second set of primary antibodies overnight at 4°C (rabbit monoclonal anti-VCAM-1 [EPR5047], Abcam ab215380—1:100; rat monoclonal anti-ICAM-1

[YN1/1.7.4], Abcam ab119871—1:100; rabbit monoclonal anti-CD3 [SP7], ThermoFisher Scientific RM-9107-S—1:100; Pericyte panel [rabbit anti-Desmin, Abcam ab15200—1:50 + rabbit anti-NG2, AB5320—1:50 + rabbit anti Smooth Muscle Actin, ThermoFisher Scientific RB9010P—1:50]). Secondary antibodies (donkey anti-rabbit IgG Alexa Fluor® 594; ThermoFisher Scientific A-21207, 1:500; donkey anti-rat IgG Alexa Fluor® 647; Jackson ImmunoResearch 712-605-153, 1:500) diluted in Dako protein-free blocking solution were applied for 60 min at room temperature, followed by DAPI staining before mounting (ProLong Gold Antifade Mountant; Life Technologies P36930). All washes were performed using TBS-T buffer (10 mM TRIS, pH 8.0, 150 mM NaCl, 0.1% Tween 20).

Snap-frozen-embedded liver samples were sectioned (thickness: 10 μm) and fixed with ice-cold methanol for 30 min at −20°C. Analogous, 4%-PFA fixed tumor samples were sectioned (thickness: 10 μm). Subsequently, samples were blocked with Dako protein-free blocking solution (ref: X0909, Dako). Combinations of primary antibody for CD9 (rabbit polyclonal; Sigma C9993—1:100) together with either anti-ICAM-1 (rat monoclonal anti-ICAM-1 [YN1/1.7.4], Abcam ab119871—1:100) or anti-MECA32 (rat monoclonal anti-mouse panendothelial cell antigen [MECA-32], BD Pharmingen™, 553849—1:100) were applied in Dako protein-free blocking solution overnight at 4°C, followed by secondary antibody incubation for 60 min at room temperature (donkey anti-rabbit IgG Alexa Fluor® 488; ThermoFisher Scientific A-21206, 1:500, donkey anti-rat IgG Alexa Fluor® 647; Jackson ImmunoResearch 712-605-153, 1:500) diluted in Dako protein-free blocking solution, followed by DAPI staining before mounting (ProLong Gold Antifade Mountant; Life Technologies P36930). All washes were performed using TBS-T buffer (10 mM TRIS, pH 8.0, 150 mM NaCl, 0.1% Tween 20). Images of entire sections were acquired either on the 3D Histech Pannoramic SCAN 150 (Budapest, Hungary) with Carl Zeiss Plan-Apochromat 20×/N.A. 0.8 objective or NanoZoomer S60 Digital slide scanner (Hamamatsu) Nikon 40×/N.A. 0.75 objective with 0.23 μm/pixel resolution or on 3i Marianas CSU-W1spinning disk confocal microscope with Carl Zeiss Plan-Apochromat 20×/N.A. 0.8 objective.

RNAscope

In situ hybridization using the RNAscope technique was performed according to the manufacturer's instruction (Advanced Cell Diagnostics [ACD]), using multiplex fluorescent Reagent Kit v2. Six-micrometer thick FFPE sections were pretreated according to the manufacturer's instruction for FFPE samples, with a 30-min target retrieval step and a 30-min incubation step with RNAscope® Protease Plus. The probe Mm-Cd9 (ACD, Mm-Cd9-C1, #430631) was used, detected with TSA® Plus Cyanine 5 (NEL745001KT; Akoya Bioscience Inc, Marlborough, MA, USA), and tissue sections were counterstained with DAPI (ACD). Images of entire sections were acquired on the NanoZoomer S60 Digital slide scanner (Hamamatsu) Nikon 20×/N.A. 0.75 objective with 0.46 μm/pixel resolution.

Image analysis

Automated image analysis was performed using custom algorithms developed in Definiens Developer XD image analysis software (Definiens, Munich, Germany; Baatz *et al*, 2009). Whole slide images were analyzed in native 3DHistech or Nanozoomer scanner file format. Viable tissue regions of interest (ROIs) were manually annotated, taking care to exclude tissue artifacts such as out of focus regions, tissue tears, and folds. Necrotic areas were excluded based on nuclear morphology and defined as areas with small-punctate nuclei and/or areas of low cell density.

Positive cell counting

In both, tumor and liver tissue sections, individual cell objects were segmented by thresholding on background corrected DAPI immunofluorescence intensity. Background correction was performed using a top-hat filter, a locally adaptive technique which normalizes pixel intensity by a neighborhood mean. The segmented positive pixels were then split into individual cells by applying a classic cell watershed segmentation routine. The boundaries of each cell were then dilated to capture cytoplasmic/cell surface marker expression. Individual cells were evaluated for CD3 positivity by measuring AF594 mean fluorescent expression within the cell boundaries.

Vascular activation analysis

In both, tumor and liver tissue sections, vasculature was segmented by thresholding on AF488-positive pixel signal. The segmented vascular objects served as the ROI to quantify activation marker expression. ICAM-1 (AF647) and VCAM-1 (AF594) positive pixels were segmented both inside and outside of vessel boundaries.

PanCK/CD8 IHC analysis

Segmentation of panCK positive tumor regions and CD8 positive DAB positive pixels was performed by a custom algorithm using HSV color thresholding and standard morphological operations in Matlab 2020b (Mathworks, Natick, MA).

Bulk RNAseq analysis

Total RNA was extracted from tissues using the RNAeasy Mini Kit (Cat. #74104, Qiagen) following the provider's recommendations. The libraries were sequenced on Illumina HiSeq4000 (Illumina). We obtained on average 26 million single-end RNA-seq reads (50 bp) per sample. Sequencing reads were aligned to the mouse genome (NCBI Build 38) using GSNAP (Wu & Nacu, 2010) version "2013-10-10", allowing a maximum of two mismatches per 50 base pair sequence (parameters: "-M 2 -n 10 -B 2 -i 1 -N 1 -w 200000 -E1 --pairmax-rna=200000 --clip-overlap"). Lastly, gene expression levels were quantified by calculating the number of reads mapped to the exons of each RefSeq gene using the HTSeqGenie R package. Transcript annotation was based on the RefSeq database NCBI Annotation Releases 104 for mouse. Read counts were scaled by library size, quantile normalized, and precision weights calculated using the "voom" R package (Law *et al*, 2014). Subsequently, differential expression analysis on the normalized count data was performed using the "limma" R package (Ritchie *et al*, 2015) by contrasting treated samples with control samples, respectively. Gene expression was considered significantly different across groups if we observed a $|\log_2\text{-fold change}| \geq 1$ (estimated from the model coefficients) associated with an FDR-adjusted *P*-value ≤ 0.05. In addition, gene expression was obtained in the form of normalized Reads Per Kilobase gene model per Million total reads (nRPKM) as described previously (Srinivasan *et al*, 2016).

Gene set enrichment score analysis

The adhesion signature was accomplished by using ssGSEA method described previously (Barbie *et al*, 2009). Genes in each sample were ranked by their absolute expression, and an enrichment score was calculated by adding the difference between a weighted Empirical Cumulative Distribution Functions (ECDF) of the genes in the signature over the ECDF of remaining genes in the sample.

Mouse liver tissue preparation for scRNAseq analysis

Livers were perfused through the inferior vena cava (IVC) with 20 ml cold EGTA solution using a 22-gauge needle. The big liver lobe was dissociated using the Liver Dissociation Kit (ref: 130-105-807, Miltenyi Biotec) following manufacturer's instructions. Samples were filtered through a 100-μm cell strainer, washed with 10 ml DMEM, and spun down at 300 *g* for 10 min at 4°C. Red blood cells were lysed using ACK lysis buffer. Samples were washed with 10 ml DMEM and filtered through a 20-μm cell strainer. For further downstream processing, 3 ml of filtered cell suspension was used and spun down at 300 *g* for 10 min at 4°C. Red blood cells were lysed for a second time using ACK lysis buffer. Samples were washed with 10 ml DMEM and spun down at 300 *g* for 10 min at 4°C. Subsequently, samples were resuspended in 3 ml 10% FBS in PBS, centrifuged again (300 *g*, 10 min at 4°C) before resuspending for final cell count in 3 ml 10% FBS.

Library prep and sequencing scRNAseq

cDNAs and libraries were prepared following the manufacturer's manual (10X Genomics). Libraries were profiled by Bioanalyzer High Sensitivity DNA kit (ref: 5067-4626, Agilent Technologies) and quantified using Kapa Library Quantification Kit (Kapa Biosystems, Wilmington, MA). Each library was sequenced in one lane of HiSeq4000 (Illumina) following the manufacturer's sequencing specification (10X Genomics).

Sequencing data were processed as described previously (Long *et al*, 2019). In short, reads were tallied and demultiplexed based on their association with cell-specific barcodes. Only barcodes with > 10K associated reads were considered for further processing. For each cell, reads were mapped to the mouse reference genomes using the same GSNAP settings as for bulk RNA, respectively. The number of transcripts per gene was quantified based on unique molecular identifiers (UMI) using reads that overlapped exonic regions in sense direction. Only cells with a mitochondrial UMI fraction < 0.25 were considered for analysis. Per-gene UMI counts were normalized by the total number of transcripts per cell and scaled by the median number of transcripts across all cells.

Data processing analysis scRANseq

Sequencing data were processed as follows: Sample demultiplexing, barcode processing, and single-cell 3′ gene counting were performed using 10X Cell Ranger (Zheng *et al*, 2017). Only cells with a mitochondrial UMI fraction < 0.25 were considered for analysis. Per-gene UMI counts were normalized by the total number of transcripts per cell, scaled by the median number of transcripts across all cells, and log-transformed for downstream analysis.

Cell clustering, visualization, and differential expression analysis were performed as prescribed in the OSCA book (https://bioconductor.org/books/release/OSCA/). We used the top 20 principal components for clustering and visualization, the 25 nearest neighbors (k = 25) for graph-based clustering, and performed marker detection using the pair-wise t-test with a log-fold change threshold of 1.

For doublet detection, we used scDblFinder::scDblFinder() function (Germain *et al*, 2020), which is based on doublet simulation. A set of simulated doublets was generated by adding transcriptional profiles of pairs of cells from neighboring clusters. The putative doublet score was calculated by comparing each cell to artificially created doublets (https://bioconductor.org/books/release/OSCA/).

Mapping the liver EC scRNAseq data onto Single-Cell Transcriptome Atlas of Murine Endothelial Cells (Data ref: Kalucka *et al*, 2020b) was performed using Seurat Unimodal UMAP Projection approach. We performed standard preprocessing (log-normalization) and identified top 2,000 variable features for both our liver EC scRNAseq data and the reference scRNAseq data. We used default parameters including the number of dimensionality (30) to identify anchors that were used to transfer cell type labels and to project the query data onto the UMAP structure of the reference (Stuart *et al*, 2019).

To characterize cells based on the activity of transcriptional programs, we performed topic modeling using functions from the CountClust R package (Dey *et al*, 2017). We evaluated a range between 2 and 15 topics for their fit using the FitGoM function. A total of nine topics were selected to represent the data after inspecting the AIC and BIC statistics. Top genes associated with each topic were identified by applying the ExtractTopFeatures function, which uses the relative gene expression profile of the GoM clusters and applies a KL-divergence-based method to obtain a list of top features that drive each of the clusters.

Gene set analysis scRANseq

We tested for the enrichment of particular gene categories to identify relevant biological processes associated with: (i) differential expression or (ii) transcriptional programs (topics), by using functions from the "clusterProfiler" R package (Wu *et al*, 2021) and the MSigDB gene set collection (Liberzon *et al*, 2011). In the case of differential expression, treated samples were contrasted with control samples, genes were ranked based on the π statistic ($\pi = \text{logFC} \times -\log_{10}(P\text{-val})$) (Xiao *et al*, 2014), and subsequently gene set enrichment was performed using the clusterProfiler::GSEA function.

Statistical analysis

GraphPad Prism 9 (http://www.graphpad.com/) was used for all the statistical analysis. Experiments were repeated at least twice. No statistical method was used to predetermine sample size. Mann–Whitney test was used for the majority of data if it is not described otherwise in the figure legends. For multiple comparisons, Kruskal–Wallis one-way ANOVA was used if it is not described otherwise in the figure legends. Simple linear regression analysis was used for correlation analysis. Data are represented as means ± SEM (standard error of the mean) of biological replicates. In all figures, statistical significance between the indicated sample and control or between marked pairs is indicated.

Data availability

All RNA-seq data are publicly available as of the date of this publication. This paper does not report original code. Any additional information required to reanalyze the data reported in this paper is available from the Lead Contact upon request. The datasets produced

in this study are available in the following databases: Superseries: T cell dependent bispecific antibodies (TDBs) promote T cell redistribution through organ-specific alteration of vascular endothelial cell GSE198869 (https://www.ncbi.nlm.nih.gov/geo/query/acc.cgi?acc=GSE198869). Subseries: T cell dependent bispecific antibodies (TDBs) promote T cell redistribution through organ-specific alteration of vascular endothelial cell (bulk RNAseq) GSE198867 (https://www.ncbi.nlm.nih.gov/geo/query/acc.cgi?acc=GSE198867). Subseries: T cell dependent bispecific antibodies (TDBs) promote T cell redistribution through organ-specific alteration of vascular endothelial cell (scRNAseq) GSE198868 (https://www.ncbi.nlm.nih.gov/geo/query/acc.cgi?acc=GSE198868).

Expanded View for this article is available online.

Acknowledgements

We thank A. Tan, C.K. Poon, T. Ho, G. Tweet, and J. Borneo for FACS support; A.P. Martinez for cytokine and chemokine analysis; L. Leong for analysis of serum samples; M. Adrian for help with image acquisition; M. Baca, C. Espiritu, and Pathology core laboratories for tissue processing and imaging; J. Preston and M. Dohse for supporting panCK/CD8 IHC dual staining development; S.J.H. Waaijer, I. Balter, and T. Juntilla for animal and reagent support; M. Chen for helpful discussion regarding scRNAseq analysis; D. Mandikian for providing supporting data; K. B. Walsh for helpful discussions; Laboratory Animal Resources for animal care; members of the Ye laboratory for discussion and comments on the manuscript. Illustrations were created with BioRender.com. This study was funded by Genentech Inc., South San Francisco, CA 94080, USA.

Author contributions

Patricia Himmels: Conceptualization; resources; data curation; formal analysis; supervision; validation; investigation; visualization; methodology; writing – original draft; project administration; writing – review and editing. **Thi Thu Thao Nguyen:** Resources; data curation; formal analysis; visualization. **Maresa Caunt Mitzner:** Conceptualization; formal analysis; investigation; methodology. **Alfonso Arrazate:** Resources; investigation. **Stacey Yeung:** Conceptualization; formal analysis; investigation; methodology. **Jeremy Burton:** Formal analysis; investigation; methodology. **Robyn Clark:** Resources; formal analysis; investigation; methodology. **Klara Totpal:** Resources; supervision. **Raj Jesudason:** Data curation; formal analysis. **Angela Yang:** Data curation; investigation. **Margaret Solon:** Data curation; investigation; methodology. **Jeffrey Eastham:** Data curation; formal analysis. **Zora Modrusan:** Resources; supervision; validation; methodology. **Joshua D Webster:** Resources; data curation; supervision; validation. **Amy A Lo:** Resources; data curation; formal analysis; supervision; validation. **Robert Piskol:** Resources; data curation; formal analysis; supervision; validation; visualization; methodology. **Weilan Ye:** Conceptualization; resources; data curation; formal analysis; supervision; validation; investigation; visualization; methodology; writing – original draft; writing – review and editing.

Disclosure and competing interests statement

All authors are employees of Genentech, a Roche subsidiary, and some of them hold Roche stocks. The authors have no additional financial interests.

References

Aird WC (2007a) Phenotypic heterogeneity of the endothelium: I. Structure, function, and mechanisms. *Circ Res* 100: 158 – 173

Aird WC (2007b) Phenotypic heterogeneity of the endothelium: II. Representative vascular beds. *Circ Res* 100: 174 – 190

Arora L, Pal D (2021) Remodeling of stromal cells and immune landscape in microenvironment during tumor progression. *Front Oncol* 11: 596798

Augustin HG, Koh GY (2017) Organotypic vasculature: from descriptive heterogeneity to functional pathophysiology. *Science* 357: eaal2379

Baatz M, Zimmermann J, Blackmore CG (2009) Automated analysis and detailed quantification of biomedical images using definiens cognition network technology. *Comb Chem High Throughput Screen* 12: 908 – 916

Bailey RL, Herbert JM, Khan K, Heath VL, Bicknell R, Tomlinson MG (2011) The emerging role of tetraspanin microdomains on endothelial cells. *Biochem Soc Trans* 39: 1667 – 1673

Barbie DA, Tamayo P, Boehm JS, Kim SY, Moody SE, Dunn IF, Schinzel AC, Sandy P, Meylan E, Scholl C *et al* (2009) Systematic RNA interference reveals that oncogenic KRAS-driven cancers require TBK1. *Nature* 462: 108 – 112

Bargou R, Leo E, Zugmaier G, Klinger M, Goebeler M, Knop S, Noppeney R, Viardot A, Hess G, Schuler M *et al* (2008) Tumor regression in cancer patients by very low doses of a T cell-engaging antibody. *Science* 321: 974 – 977

Barreiro O, Yanez-Mo M, Sala-Valdes M, Gutierrez-Lopez MD, Ovalle S, Higginbottom A, Monk PN, Cabanas C, Sanchez-Madrid F (2005) Endothelial tetraspanin microdomains regulate leukocyte firm adhesion during extravasation. *Blood* 105: 2852 – 2861

Barreiro O, Zamai M, Yanez-Mo M, Tejera E, Lopez-Romero P, Monk PN, Gratton E, Caiolfa VR, Sanchez-Madrid F (2008) Endothelial adhesion receptors are recruited to adherent leukocytes by inclusion in preformed tetraspanin nanoplatforms. *J Cell Biol* 183: 527 – 542

Berraondo P, Sanmamed MF, Ochoa MC, Etxeberria I, Aznar MA, Perez-Gracia JL, Rodriguez-Ruiz ME, Ponz-Sarvise M, Castanon E, Melero I (2019) Cytokines in clinical cancer immunotherapy. *Br J Cancer* 120: 6 – 15

Brentjens RJ, Davila ML, Riviere I, Park J, Wang X, Cowell LG, Bartido S, Stefanski J, Taylor C, Olszewska M *et al* (2013) CD19-targeted T cells rapidly induce molecular remissions in adults with chemotherapy-refractory acute lymphoblastic leukemia. *Sci Transl Med* 5: 177ra138

Brudno JN, Kochenderfer JN (2016) Toxicities of chimeric antigen receptor T cells: recognition and management. *Blood* 127: 3321 – 3330

Carman CV, Martinelli R (2015) T lymphocyte-endothelial interactions: emerging understanding of trafficking and antigen-specific immunity. *Front Immunol* 6: 603

Chen PL, Roh W, Reuben A, Cooper ZA, Spencer CN, Prieto PA, Miller JP, Bassett RL, Gopalakrishnan V, Wani K *et al* (2016) Analysis of immune signatures in longitudinal tumor samples yields insight into biomarkers of response and mechanisms of resistance to immune checkpoint blockade. *Cancer Discov* 6: 827 – 837

Ciciola P, Cascetta P, Bianco C, Formisano L, Bianco R (2020) Combining immune checkpoint inhibitors with anti-angiogenic agents. *J Clin Med* 9: 675

Collins T (1993) Endothelial nuclear factor-kappa B and the initiation of the atherosclerotic lesion. *Lab Invest* 68: 499 – 508

Dahlen E, Veitonmaki N, Norlen P (2018) Bispecific antibodies in cancer immunotherapy. *Ther Adv Vaccines Immunother* 6: 3 – 17

Dey KK, Hsiao CJ, Stephens M (2017) Visualizing the structure of RNA-seq expression data using grade of membership models. *PLoS Genet* 13: e1006599

Fiedler U, Augustin HG (2006) Angiopoietins: a link between angiogenesis and inflammation. *Trends Immunol* 27: 552 – 558

Franz J, Brinkmann BF, Konig M, Huve J, Stock C, Ebnet K, Riethmuller C (2016) Nanoscale imaging reveals a tetraspanin-CD9 coordinated elevation of endothelial ICAM-1 clusters. *PLoS One* 11: e0146598

Fries JW, Williams AJ, Atkins RC, Newman W, Lipscomb MF, Collins T (1993) Expression of VCAM-1 and E-selectin in an *in vivo* model of endothelial activation. *Am J Pathol* 143: 725 – 737

Fukumura D, Kloepper J, Amoozgar Z, Duda DG, Jain RK (2018) Enhancing cancer immunotherapy using antiangiogenics: opportunities and challenges. *Nat Rev Clin Oncol* 15: 325 – 340

Germain PL, Sonrel A, Robinson MD (2020) pipeComp, a general framework for the evaluation of computational pipelines, reveals performant single cell RNA-seq preprocessing tools. *Genome Biol* 21: 227

Grauel AL, Nguyen B, Ruddy D, Laszewski T, Schwartz S, Chang J, Chen J, Piquet M, Pelletier M, Yan Z *et al* (2020) TGFbeta-blockade uncovers stromal plasticity in tumors by revealing the existence of a subset of interferon-licensed fibroblasts. *Nat Commun* 11: 6315

Gust J, Hay KA, Hanafi LA, Li D, Myerson D, Gonzalez-Cuyar LF, Yeung C, Liles WC, Wurfel M, Lopez JA *et al* (2017) Endothelial activation and blood-brain barrier disruption in neurotoxicity after adoptive immunotherapy with CD19 CAR-T cells. *Cancer Discov* 7: 1404 – 1419

Gust J, Ponce R, Liles WC, Garden GA, Turtle CJ (2020) Cytokines in CAR T cell-associated neurotoxicity. *Front Immunol* 11: 577027

Han X, Wang R, Zhou Y, Fei L, Sun H, Lai S, Saadatpour A, Zhou Z, Chen H, Ye F *et al* (2018) Mapping the mouse cell atlas by microwell-seq. *Cell* 172: e1017

Hay KA, Hanafi LA, Li D, Gust J, Liles WC, Wurfel MM, Lopez JA, Chen J, Chung D, Harju-Baker S *et al* (2017) Kinetics and biomarkers of severe cytokine release syndrome after CD19 chimeric antigen receptor-modified T cell therapy. *Blood* 130: 2295 – 2306

Hegde PS, Chen DS (2020) Top 10 challenges in cancer immunotherapy. *Immunity* 52: 17 – 35

Hosseini SS, Khalili S, Baradaran B, Bidar N, Shahbazi MA, Mosafer J, Hashemzaei M, Mokhtarzadeh A, Hamblin MR (2021) Bispecific monoclonal antibodies for targeted immunotherapy of solid tumors: recent advances and clinical trials. *Int J Biol Macromol* 167: 1030 – 1047

Ji RR, Chasalow SD, Wang L, Hamid O, Schmidt H, Cogswell J, Alaparthy S, Berman D, Jure-Kunkel M, Siemers NO *et al* (2012) An immune-active tumor microenvironment favors clinical response to ipilimumab. *Cancer Immunol Immunother* 61: 1019 – 1031

Junttila TT, Li J, Johnston J, Hristopoulos M, Clark R, Ellerman D, Wang BE, Li Y, Mathieu M, Li G *et al* (2014) Antitumor efficacy of a bispecific antibody that targets HER2 and activates T cells. *Cancer Res* 74: 5561 – 5571

Kalos M, Levine BL, Porter DL, Katz S, Grupp SA, Bagg A, June CH (2011) T cells with chimeric antigen receptors have potent antitumor effects and can establish memory in patients with advanced leukemia. *Sci Transl Med* 3: 95ra73

Kalucka J, de Rooij L, Goveia J, Rohlenova K, Dumas SJ, Meta E, Conchinha NV, Taverna F, Teuwen LA, Veys K *et al* (2020a) Single-cell transcriptome atlas of murine endothelial cells. *Cell* 180: 764 – 779

Kalucka J, de Rooij LPMH, Goveia J, Rohlenova K, Dumas SJ, Meta E, Conchinha NV, Taverna F, Teuwen LA, Veys K *et al* (2020b) ArrayExpress E-MTAB-8077 (https://www.ebi.ac.uk/biostudies/arrayexpress/studies/E-MTAB-8077). [DATASET]

Kantarjian H, Stein A, Gokbuget N, Fielding AK, Schuh AC, Ribera JM, Wei A, Dombret H, Foa R, Bassan R *et al* (2017) Blinatumomab versus chemotherapy for advanced acute lymphoblastic leukemia. *N Engl J Med* 376: 836 – 847

Kochenderfer JN, Dudley ME, Feldman SA, Wilson WH, Spaner DE, Maric I, Stetler-Stevenson M, Phan GQ, Hughes MS, Sherry RM *et al* (2012) B-cell depletion and remissions of malignancy along with cytokine-associated toxicity in a clinical trial of anti-CD19 chimeric-antigen-receptor-transduced T cells. *Blood* 119: 2709 – 2720

Lambrechts D, Wauters E, Boeckx B, Aibar S, Nittner D, Burton O, Bassez A, Decaluwe H, Pircher A, Van den Eynde K *et al* (2018) Phenotype molding of stromal cells in the lung tumor microenvironment. *Nat Med* 24: 1277 – 1289

Law CW, Chen Y, Shi W, Smyth GK (2014) voom: precision weights unlock linear model analysis tools for RNA-seq read counts. *Genome Biol* 15: R29

Lee WS, Yang H, Chon HJ, Kim C (2020) Combination of anti-angiogenic therapy and immune checkpoint blockade normalizes vascular-immune crosstalk to potentiate cancer immunity. *Exp Mol Med* 52: 1475 – 1485

Lewis Phillips GD, Li G, Dugger DL, Crocker LM, Parsons KL, Mai E, Blattler WA, Lambert JM, Chari RV, Lutz RJ *et al* (2008) Targeting HER2-positive breast cancer with trastuzumab-DM1, an antibody-cytotoxic drug conjugate. *Cancer Res* 68: 9280 – 9290

Li J, Stagg NJ, Johnston J, Harris MJ, Menzies SA, DiCara D, Clark V, Hristopoulos M, Cook R, Slaga D *et al* (2017) Membrane-proximal epitope facilitates efficient T cell synapse formation by anti-FcRH5/CD3 and is a requirement for myeloma cell killing. *Cancer Cell* 31: 383 – 395

Li J, Ybarra R, Mak J, Herault A, De Almeida P, Arrazate A, Ziai J, Totpal K, Junttila MR, Walsh KB *et al* (2018) IFNgamma-induced chemokines are required for CXCR3-mediated T cell recruitment and antitumor efficacy of anti-HER2/CD3 bispecific antibody. *Clin Cancer Res* 24: 6447 – 6458

Li J, Piskol R, Ybarra R, Chen YJ, Li J, Slaga D, Hristopoulos M, Clark R, Modrusan Z, Totpal K *et al* (2019) CD3 bispecific antibody-induced cytokine release is dispensable for cytotoxic T cell activity. *Sci Transl Med* 11: eaax8861

Liao JK (2013) Linking endothelial dysfunction with endothelial cell activation. *J Clin Invest* 123: 540 – 541

Liberzon A, Subramanian A, Pinchback R, Thorvaldsdottir H, Tamayo P, Mesirov JP (2011) Molecular Signatures Database (MSigDB) 3.0. *Bioinformatics* 27: 1739 – 1740

Liberzon A, Birger C, Thorvaldsdottir H, Ghandi M, Mesirov JP, Tamayo P (2015) The Molecular Signatures Database (MSigDB) hallmark gene set collection. *Cell Syst* 1: 417 – 425

Lo AA, Johnston J, Li J, Mandikian D, Hristopoulos M, Clark R, Nickles D, Liang WC, Hotzel K, Dunlap D *et al* (2021) Anti-LYPD1/CD3 T cell-dependent bispecific antibody for the treatment of ovarian cancer. *Mol Cancer Ther* 20: 716 – 725

Long JE, Wongchenko MJ, Nickles D, Chung WJ, Wang BE, Riegler J, Li J, Li Q, Sandoval W, Eastham-Anderson J *et al* (2019) Therapeutic resistance and susceptibility is shaped by cooperative multi-compartment tumor adaptation. *Cell Death Differ* 26: 2416 – 2429

Maude SL, Frey N, Shaw PA, Aplenc R, Barrett DM, Bunin NJ, Chew A, Gonzalez VE, Zheng Z, Lacey SF *et al* (2014) Chimeric antigen receptor T cells for sustained remissions in leukemia. *N Engl J Med* 371: 1507 – 1517

Metzemaekers M, Vanheule V, Janssens R, Struyf S, Proost P (2017) Overview of the mechanisms that may contribute to the non-redundant activities of interferon-inducible CXC chemokine receptor 3 ligands. *Front Immunol* 8: 1970

Miller JF, Sadelain M (2015) The journey from discoveries in fundamental immunology to cancer immunotherapy. *Cancer Cell* 27: 439 – 449

Okegawa T, Pong RC, Li Y, Hsieh JT (2004) The role of cell adhesion molecule in cancer progression and its application in cancer therapy. *Acta Biochim Pol* 51: 445 – 457

Park S, Nedrow JR, Josefsson A, Sgouros G (2017) Human HER2 overexpressing mouse breast cancer cell lines derived from MMTV.f.HuHER2 mice:

characterization and use in a model of metastatic breast cancer. *Oncotarget* 8: 68071 – 68082

Patel AP, Tirosh I, Trombetta JJ, Shalek AK, Gillespie SM, Wakimoto H, Cahill DP, Nahed BV, Curry WT, Martuza RL *et al* (2014) Single-cell RNA-seq highlights intratumoral heterogeneity in primary glioblastoma. *Science* 344: 1396 – 1401

Peng D, Kryczek I, Nagarsheth N, Zhao L, Wei S, Wang W, Sun Y, Zhao E, Vatan L, Szeliga W *et al* (2015) Epigenetic silencing of TH1-type chemokines shapes tumour immunity and immunotherapy. *Nature* 527: 249 – 253

Pockaj BA, Sherry RM, Wei JP, Yannelli JR, Carter CS, Leitman SF, Carasquillo JA, Steinberg SM, Rosenberg SA, Yang JC (1994) Localization of 111indium-labeled tumor infiltrating lymphocytes to tumor in patients receiving adoptive immunotherapy. Augmentation with cyclophosphamide and correlation with response. *Cancer* 73: 1731 – 1737

Potente M, Makinen T (2017) Vascular heterogeneity and specialization in development and disease. *Nat Rev Mol Cell Biol* 18: 477 – 494

Qiu Y, Su M, Liu L, Tang Y, Pan Y, Sun J (2021) Clinical application of cytokines in cancer immunotherapy. *Drug Des Devel Ther* 15: 2269 – 2287

R Core Team (2020) *R: a language and environment for statistical computing*. Vienna, Austria: R Foundation for Statistical Computing

Reyes R, Cardenes B, Machado-Pineda Y, Cabanas C (2018) Tetraspanin CD9: a key regulator of cell adhesion in the immune system. *Front Immunol* 9: 863

Ritchie ME, Phipson B, Wu D, Hu Y, Law CW, Shi W, Smyth GK (2015) Limma powers differential expression analyses for RNA-sequencing and microarray studies. *Nucleic Acids Res* 43: e47

Scholz A, Plate KH, Reiss Y (2015) Angiopoietin-2: a multifaceted cytokine that functions in both angiogenesis and inflammation. *Ann NY Acad Sci* 1347: 45 – 51

Spranger S, Bao R, Gajewski TF (2015) Melanoma-intrinsic beta-catenin signalling prevents anti-tumour immunity. *Nature* 523: 231 – 235

Srinivasan K, Friedman BA, Larson JL, Lauffer BE, Goldstein LD, Appling LL, Borneo J, Poon C, Ho T, Cai F *et al* (2016) Untangling the brain's neuroinflammatory and neurodegenerative transcriptional responses. *Nat Commun* 7: 11295

Staflin K, Zuch de Zafra CL, Schutt LK, Clark V, Zhong F, Hristopoulos M, Clark R, Li J, Mathieu M, Chen X *et al* (2020) Target arm affinities determine preclinical efficacy and safety of anti-HER2/CD3 bispecific antibody. *JCI Insight* 5: e133757

Stuart T, Butler A, Hoffman P, Hafemeister C, Papalexi E, Mauck WM 3rd, Hao Y, Stoeckius M, Smibert P, Satija R (2019) Comprehensive integration of single-cell data. *Cell* 177: 1888 – 1902

Subramanian A, Tamayo P, Mootha VK, Mukherjee S, Ebert BL, Gillette MA, Paulovich A, Pomeroy SL, Golub TR, Lander ES *et al* (2005) Gene set enrichment analysis: a knowledge-based approach for interpreting genome-wide expression profiles. *Proc Natl Acad Sci USA* 102: 15545 – 15550

Sun LL, Ellerman D, Mathieu M, Hristopoulos M, Chen X, Li Y, Yan X, Clark R, Reyes A, Stefanich E *et al* (2015) Anti-CD20/CD3 T cell-dependent bispecific antibody for the treatment of B cell malignancies. *Sci Transl Med* 7: 287ra270

Teachey DT, Rheingold SR, Maude SL, Zugmaier G, Barrett DM, Seif AE, Nichols KE, Suppa EK, Kalos M, Berg RA *et al* (2013) Cytokine release syndrome after blinatumomab treatment related to abnormal macrophage activation and ameliorated with cytokine-directed therapy. *Blood* 121: 5154 – 5157

Teachey DT, Lacey SF, Shaw PA, Melenhorst JJ, Maude SL, Frey N, Pequignot E, Gonzalez VE, Chen F, Finklestein J *et al* (2016) Identification of predictive biomarkers for cytokine release syndrome after chimeric antigen receptor T cell therapy for acute lymphoblastic leukemia. *Cancer Discov* 6: 664 – 679

Topp MS, Kufer P, Gokbuget N, Goebeler M, Klinger M, Neumann S, Horst HA, Raff T, Viardot A, Schmid M *et al* (2011) Targeted therapy with the T cell-engaging antibody blinatumomab of chemotherapy-refractory minimal residual disease in B-lineage acute lymphoblastic leukemia patients results in high response rate and prolonged leukemia-free survival. *J Clin Oncol* 29: 2493 – 2498

Trivedi A, Stienen S, Zhu M, Li H, Yuraszeck T, Gibbs J, Heath T, Loberg R, Kasichayanula S (2017) Clinical pharmacology and translational aspects of bispecific antibodies. *Clin Transl Sci* 10: 147 – 162

Turtle CJ, Hanafi LA, Berger C, Hudecek M, Pender B, Robinson E, Hawkins R, Chaney C, Cherian S, Chen X *et al* (2016) Immunotherapy of non-Hodgkin's lymphoma with a defined ratio of $CD8^+$ and $CD4^+$ CD19-specific chimeric antigen receptor-modified T cells. *Sci Transl Med* 8: 355ra116

Ventola CL (2017a) Cancer immunotherapy, part 2: efficacy, safety, and other clinical considerations. *P T* 42: 452 – 463

Ventola CL (2017b) Cancer immunotherapy, part 3: challenges and future trends. *P T* 42: 514 – 521

Wang G, Lu X, Dey P, Deng P, Wu CC, Jiang S, Fang Z, Zhao K, Konaparthi R, Hua S *et al* (2016) Targeting YAP-dependent MDSC infiltration impairs tumor progression. *Cancer Discov* 6: 80 – 95

Wu TD, Nacu S (2010) Fast and SNP-tolerant detection of complex variants and splicing in short reads. *Bioinformatics* 26: 873 – 881

Wu T, Hu E, Xu S, Chen M, Guo P, Dai Z, Feng T, Zhou L, Tang W, Zhan L *et al* (2021) clusterProfiler 4.0: a universal enrichment tool for interpreting omics data. *Innovation* 2: 100141

Xiao Y, Hsiao TH, Suresh U, Chen HI, Wu X, Wolf SE, Chen Y (2014) A novel significance score for gene selection and ranking. *Bioinformatics* 30: 801 – 807

Yu S, Li A, Liu Q, Yuan X, Xu H, Jiao D, Pestell RG, Han X, Wu K (2017) Recent advances of bispecific antibodies in solid tumors. *J Hematol Oncol* 10: 155

Zhao Q, Eichten A, Parveen A, Adler C, Huang Y, Wang W, Ding Y, Adler A, Nevins T, Ni M *et al* (2018) Single-cell transcriptome analyses reveal endothelial cell heterogeneity in tumors and changes following antiangiogenic treatment. *Cancer Res* 78: 2370 – 2382

Zhao Q, Molina-Portela MDP, Parveen A, Adler A, Adler C, Hock E, Wang W, Ni M, Wei Y, Atwal G *et al* (2020) Heterogeneity and chimerism of endothelial cells revealed by single-cell transcriptome in orthotopic liver tumors. *Angiogenesis* 23: 581 – 597

Zheng GX, Terry JM, Belgrader P, Ryvkin P, Bent ZW, Wilson R, Ziraldo SB, Wheeler TD, McDermott GP, Zhu J *et al* (2017) Massively parallel digital transcriptional profiling of single cells. *Nat Commun* 8: 14049

Expanded View Figures

Figure EV1. The observed systemic effects of TDB treatment are largely acute and transient.

A Serum cytokine levels from control-treated (black) and anti-HER2/CD3 TDB-treated (red) mice, 4 days post treatment ($n = 8$ mice/treatment).

B Gating strategy for flow cytometry analysis of circulating immune cells. Singlets are gated based on forward scatter area (FSC-A) versus forward scatter height (FSC-H). $CD45^+$ cells are gated from viable cells, and T cells are sub-divided as $CD8^+$ versus $CD4^+$ T cells from viable cells and $CD45^+$ cells.

C Quantification of $CD4^+$ (top panel) and $CD8^+$ (bottom panel) T cell counts in peripheral blood samples from mice treated with control (black) or anti-HER2/CD3 TDB (red), 4 days post treatment ($n = 8$ mice/treatment).

D Gating strategy for flow cytometry analysis of immune cells in dissociated tissue samples. Singlets are gated based on forward scatter area (FSC-A) versus forward scatter height (FSC-H). $CD45^+$ cells are gated from viable cells and T cells are sub-divided as $CD8^+$ versus $CD4^+$ T cells from viable cells and $CD45^+$ cells.

E, F Representative dual chromogenic IHC for CD8a and pan-cytokeratin (AE1/AE3) staining of Founder5 tumor sections (E) or liver sections (F) from vehicle control-treated and anti-HER2/CD3 TDB-treated mice (top panels). Scale bar = 1,000 μm. Insets show enlarged view of the boxed area. Scale bar of insets = 100 μm. Quantification of $CD8^+$ cell counts in Founder5 whole tumor sections normalized to tumor tissue areas (E) or liver sections normalized to tissue areas (F), 24 h ($n = 9$ mice/treatment) or 4 days post treatment ($n = 8$ mice/treatment) (bottom panels).

G Serum levels of alanine transaminase (ALT, top panel) and aspartate aminotransferase (AST, bottom panel) from control-treated (black) and anti-HER2/CD3 TDB-treated (red) mice, 6 h, 24 h, and 4 days post treatment ($n = 5$–9 mice/treatment).

H, I Tumor (H) or liver (I) tissue cytokine levels normalized to total protein concentration from control-treated (black) and anti-HER2/CD3 TDB-treated (red) mice, 4 days post treatment ($n = 6$/7 mice/treatment).

Data information: Black = control-treated mice. Red = anti-HER2/CD3 TDB-treated mice. Mann–Whitney test was run to determine *P*-values for experiments with two groups, and Kruskal–Wallis one-way ANOVA was used for multiple groups. Data are shown as means ± SEM.
Source data are available online for this figure.

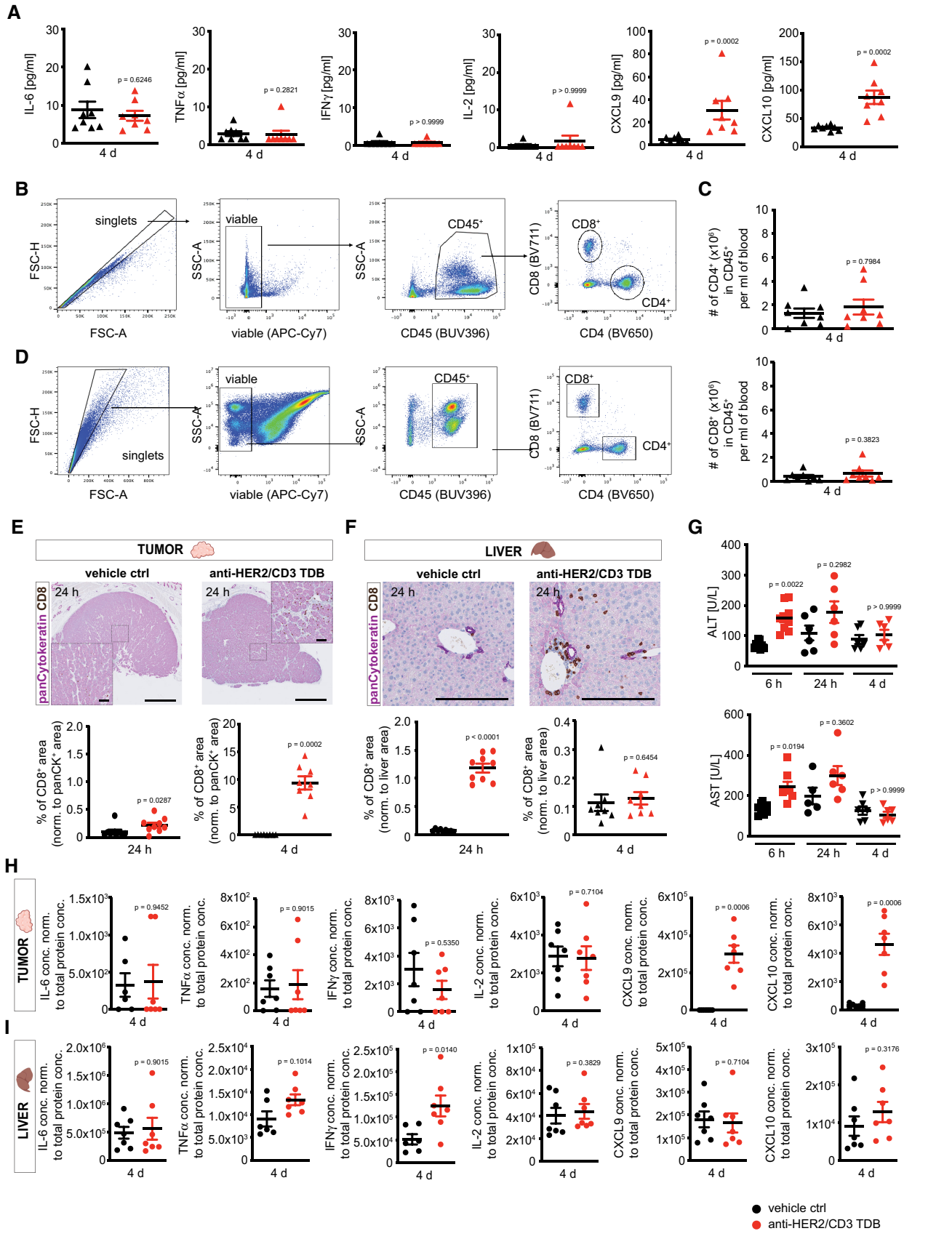

Figure EV1.

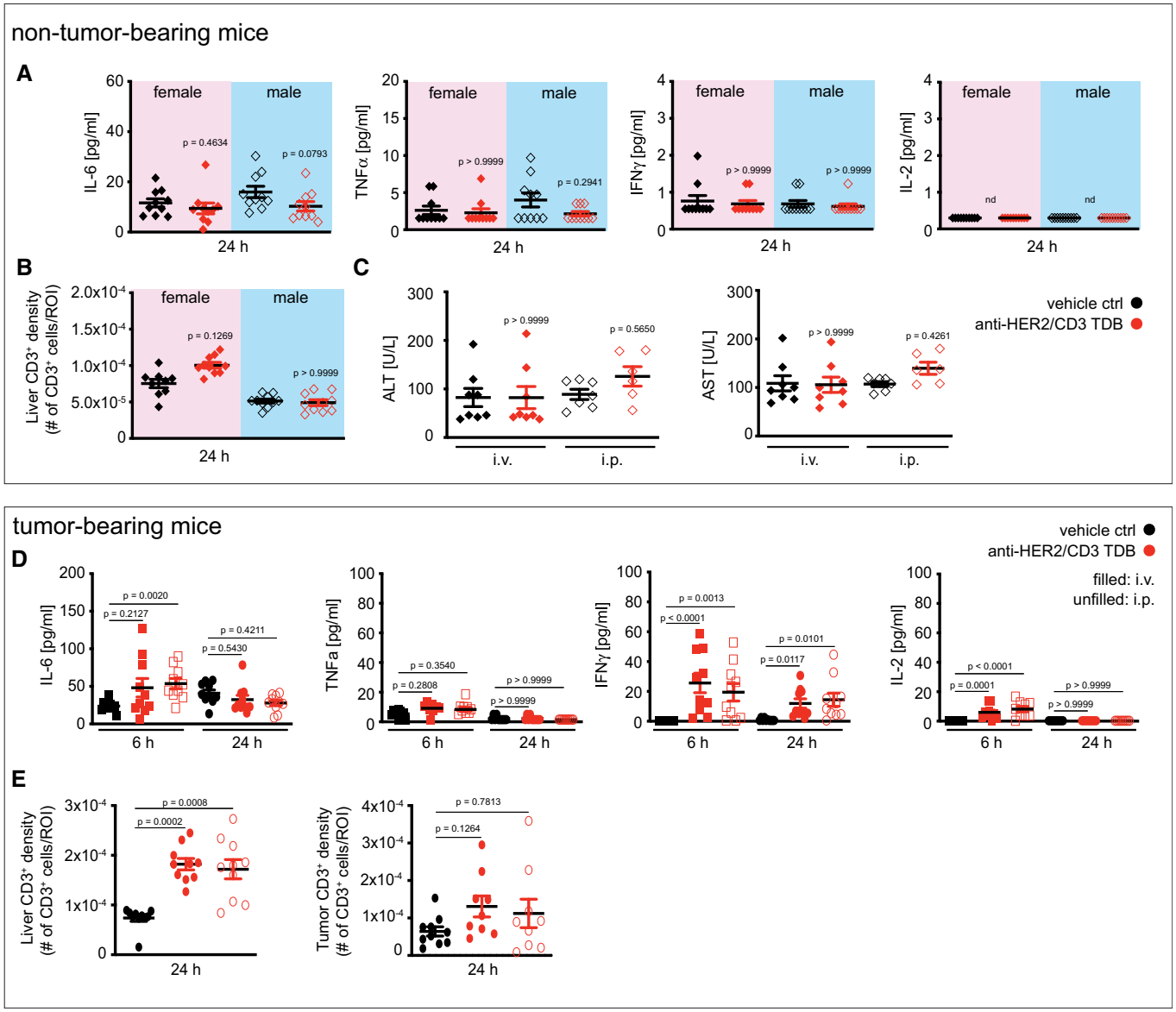

Figure EV2. The observed effects of TDB treatment are dependent on the engagement of TDB with T cells and tumor antigen.

A Serum cytokine levels from control-treated (black) and anti-HER2/CD3 TDB-treated (red) non-tumor-bearing mice, 24 h post treatment ($n = 10$ mice/treatment) in female (left, rose-shaded) and male (right, blue-shaded). Kruskal–Wallis one-way ANOVA analysis showed no difference between groups. nd, not detected.

B Quantification of $CD3^+$ cell counts in liver sections normalized to tissue areas from control-treated (black) and anti-HER2/CD3 TDB-treated (red) non-tumor-bearing mice, 24 h post treatment ($n = 9/10$ mice/treatment). Kruskal–Wallis one-way ANOVA analysis showed no difference between groups.

C Serum levels of alanine transaminase (ALT, left) and aspartate aminotransferase (AST, right) from control-treated (black) and anti-HER2/CD3 TDB-treated (red) non-tumor-bearing mice, 24 h post treatment ($n = 6–8$ mice/treatment), comparing intravenous (i.v., filled symbols) and intraperitoneal (i.p., unfilled symbols) injections.

D Serum cytokine levels from control-treated (black) and anti-HER2/CD3 TDB-treated (red) tumor-bearing mice, 6 h and 24 h post treatment ($n = 9/10$ mice/treatment), comparing intravenous (i.v., filled symbols) and intraperitoneal (i.p., unfilled symbols) injections. Kruskal–Wallis one-way ANOVA analysis showed no difference between groups.

E Quantification of $CD3^+$ cell counts in Founder5 liver (left) and tumor (right) sections normalized to tissue areas from control-treated (black) and anti-HER2/CD3 TDB-treated (red) mice, 24 h post treatment ($n = 9/10$ mice/treatment), comparing intravenous (i.v., filled symbols) and intraperitoneal (i.p., unfilled symbols) injections. Kruskal–Wallis one-way ANOVA analysis showed no difference between groups.

Data information: Black = control-treated mice. Red = anti-HER2/CD3 TDB-treated mice. Kruskal–Wallis one-way ANOVA was used for multiple groups. Data are shown as means ± SEM.
Source data are available online for this figure.

Figure EV3. TDB treatment effects are independent of tumor model and TDB used.

A Serum cytokine levels from control-treated (black) and anti-LYPD1/CD3 TDB-treated (purple) tumor-bearing mice from the ID8/LYPD1X4 ovarian cancer model, 6 h, 24 h, and 4 days post treatment ($n = 8$ mice/treatment).

B Quantification of $CD4^+$ (top panel) and $CD8^+$ (bottom panel) T cell counts in peripheral blood samples from mice treated with control (black, $n = 8$) or anti-LYPD1/CD3 TDB (purple, $n = 8$), 24 h post treatment.

C, D Representative images of ID8/LYPD1X4 tumor sections (C, left) or liver sections (D, left) stained with CD3 (red), Endomucin (white), and DAPI (blue) 24 h post treatment (top panels). Scale bar = 200 μm. Quantification of $CD3^+$ cell counts in ID8/LYPD1X4 whole tumor sections (C) or liver sections (D) normalized to tissue areas 24 h and 4 days post treatment ($n = 8$ mice/treatment) (bottom panels).

E Serum levels of alanine transaminase (ALT, top panel) and aspartate aminotransferase (AST, bottom panel) from control-treated (black) and anti-LYPD1/CD3 TDB-treated (purple) mice, 24 h and 4 days post treatment ($n = 7$–8 mice/treatment).

F, G Quantification of vascular ICAM-1^+ (ICAM-1^+ Endomucin$^+$) and vascular VCAM-1^+ (VCAM-1^+ Endomucin$^+$) areas in tumor sections (F) and liver sections (G) normalized to tissue areas from control-treated (black) and anti-LYPD1/CD3 TDB-treated (purple) mice, 24 h post treatment ($n = 6$–8 mice/treatment).

Data information: Black = control-treated mice. Purple = anti-LYPD1/CD3 TDB-treated mice. Mann–Whitney test was run to determine *P*-values for experiments with two groups; Kruskal–Wallis one-way ANOVA was used for multiple groups. Data are shown as means ± SEM. ROI, region of interest.
Source data are available online for this figure.

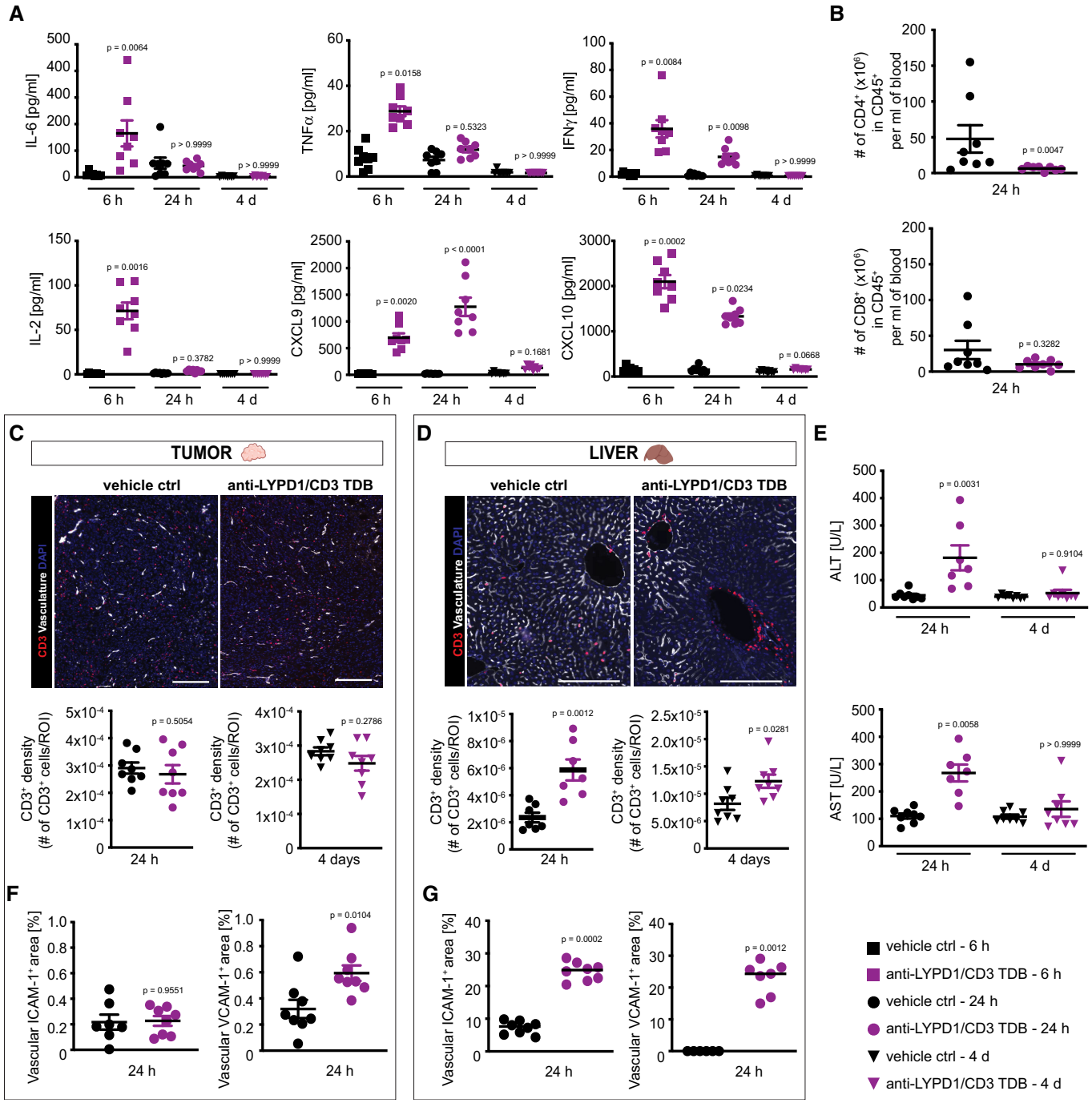

Figure EV3.

Figure EV4. Anti-HER2/CD3 TDB treatment induces dramatic transcriptional changes in the liver but does not change EC subpopulation identities.

A t-SNE plot with color-coded clusters of liver cells shown per replicate (left). Right panel shows relative abundance of detected cell types per sample. No batch effect was detected.

B t-SNE plot highlighting expression levels of selected cell type markers in the liver.

C Heatmap of selected established cell type markers.

D Calculated DoubletScore levels are shown as t-SNE plot (left) or as box plot (right). Boxes represent interquartile ranges (IQR); medians are lines in the boxes. Whiskers above and below the boxes are the lowest and highest values within 1.5 times IQR. Outliers are shown as circle beyond the whiskers.

E UMAP plot of endothelial cells color-coded for mouse organs/tissues based on reference dataset (Data ref: Kalucka *et al*, 2020b) and annotation (left) and our data mapped into the same UMAP space (right, # indicates the number of cells that mapped into the indicated organ transcriptional profile), confirming the origin of our endothelial cells being liver.

Source data are available online for this figure.

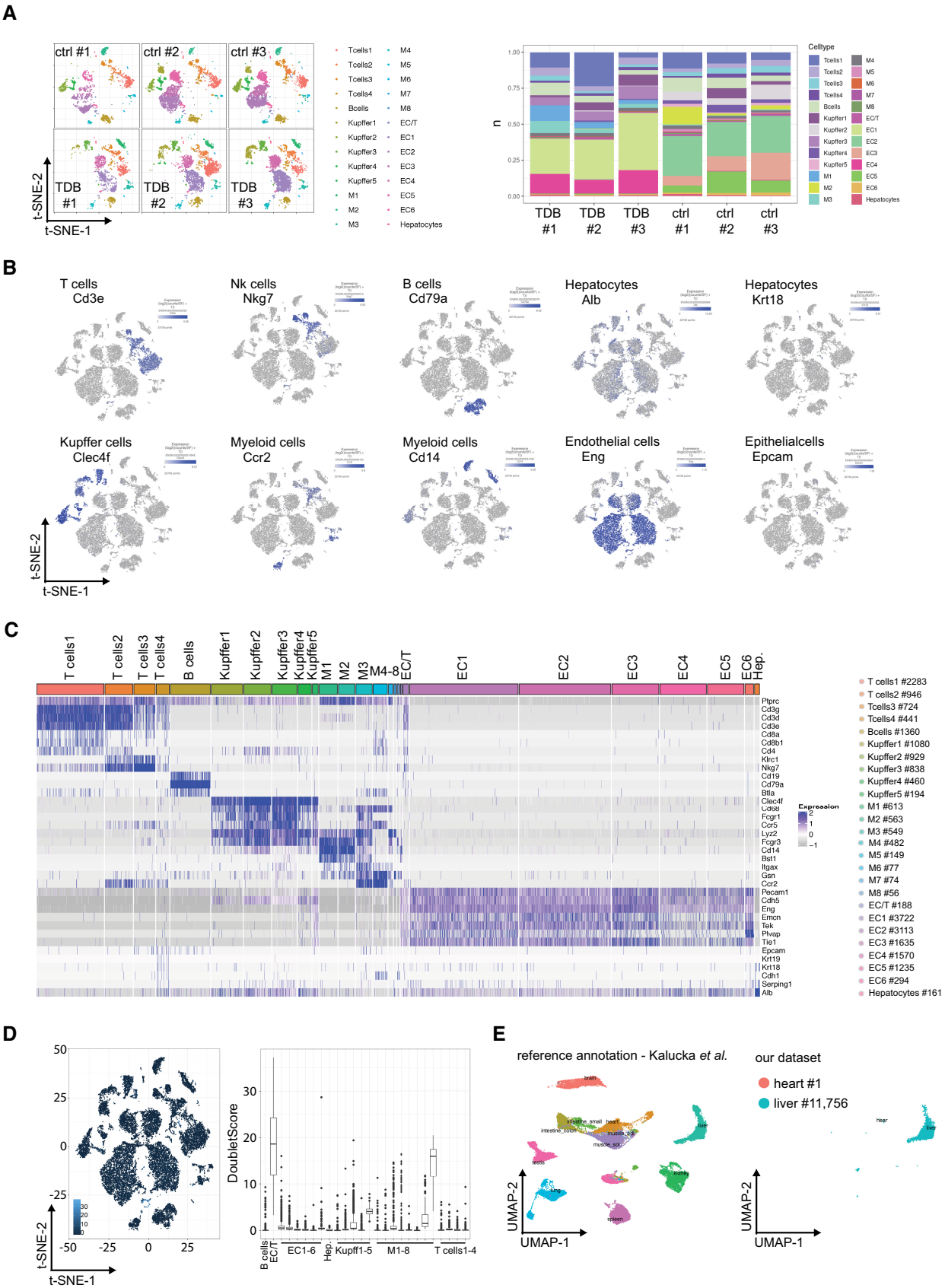

Figure EV4.

Figure EV5. Topic modeling captures the transcriptional dynamics within the different EC subtypes with and without TDB treatment.

A UMAP plot showing the relative expression levels for the nine topics based on topic modeling.

B Box plots showing the relative expression levels for the nine topics based on topic modeling across the previous identified 12 EC sub-clusters. Boxes represent interquartile ranges (IQR); medians are lines in the boxes. Whiskers above and below the boxes are the lowest and highest values within 1.5 times IQR.

Source data are available online for this figure.

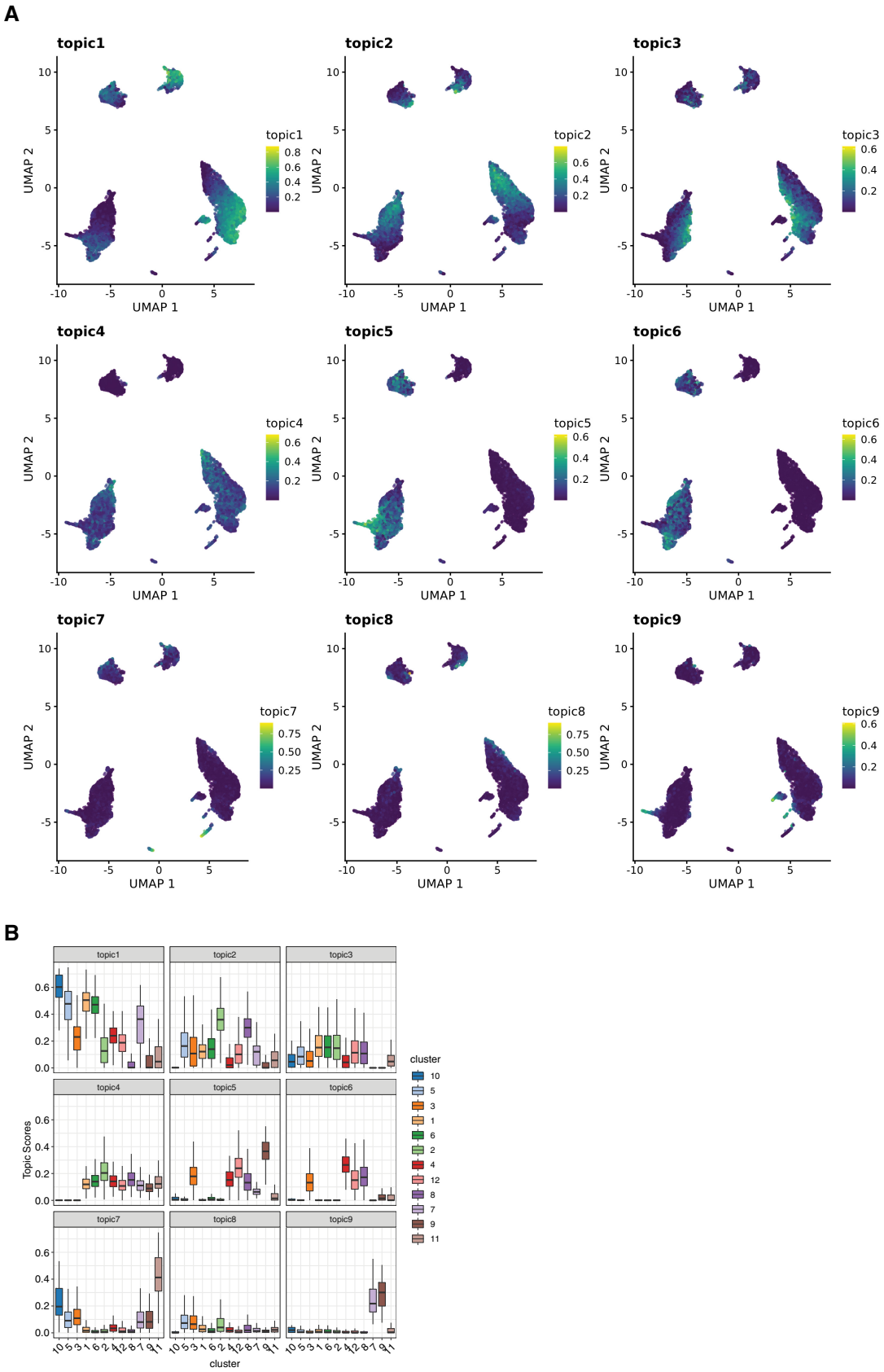

Figure EV5.